Advances in Computational Science and Engineering

doi:10.3934/acse.2023005

FINITE ELEMENTS AND FINITE VOLUMES METHODS IN WIND ENGINEERING APPLICATIONS

Hosam AlSofi,[1] Antonia Larese,[2,3] Iván Padilla,[4]
Riccardo Rossi,[5] Roberto Scotta [2] and Roland Wüchner*[6]

[1]Technische Universität München, Munich, Germany

[2]Università degli Studi di Padova, Padova, Italy

[3]Institute for Advanced Study Technical University of Munich, Garching, Germany

[4]Universidad Politécnica de Madrid, Madrid, Spain

[5]International Center for Numerical Methods in Engineering (CIMNE),
Universitat Politècnica de Catalunya, Barcelona, Spain

[6]Technische Universität Braunschweig, Braunschweig, Germany

(Communicated by Annalisa Quaini)

Abstract. In view of the importance of understanding and predicting the effects of wind on wide-span membranes and inflatable structures, a complementary experimental-numerical campaign was conducted to demonstrate the physical importance of numerical simulations in this field and to discuss relevant modeling aspects. This work aims, on the one hand, to examine the effects of some main CFD modeling decisions, such as mesh resolution, turbulence modeling, wall functions, etc., on the accuracy of simulation results. On the other hand, to compare the two most popular CFD numerical technologies (Finite Volumes and Finite Elements Methods), using the open-source frameworks OpenFOAM and Kratos Multiphysics, respectively. This parametric study and cross-validation will contribute to the ultimate goal of obtaining practical and reliable predictive numerical simulations in the field of wind engineering. This paper discusses the numerical modeling approaches of the first and fundamental step of a systematic chain of test cases, performed experimentally. It focuses on the case where a constant uniform flow and a rigid inflatable membrane structure are considered. Further extensions will include ABL flow scenarios and fluid-structure interaction.

2020 *Mathematics Subject Classification.* Primary: 65M22, 65M60; Secondary: 76D05, 74F10.

Key words and phrases. Computational Wind Engineering, Large Eddy Simulation, Detached Eddy Simulation, Variational Multiscale, Finite Volume Method, Finite Element Method, Modeling Aspects in CWE, Lightweight Structures.

*Corresponding author: Roland Wüchner.

Nomenclature.

ρ	Density, kg/m^3
p	Pressure, Pa
C_p	Pressure coefficient
μ	Dynamic viscosity, Pa $\cdot$ s
u_x	Velocity component along the x coordinate, m/s
u_y	Velocity component along the y coordinate, m/s
u_z	Velocity component along the z coordinate, m/s
$\mathbf{u}$	Velocity vector, $\mathbf{u} = [u_x, u_y, u_z]$
y^+	Dimensionless wall distance
q	Test function for the continuity equation
$\mathbf{w}$	Test function for the momentum equation
Ω	Fluid domain
$\mathbf{n}$	Unit vector normal to a given boundary
t	Time, s

1. Introduction.

Lightweight membrane structures are becoming more and more popular pushing the need for novel tools to reliably estimate wind loads and their effect on the structure. In contrast to typical relatively-stiff structures, membranes and inflatable structures are so sensitive to wind effects that conventional approaches, based on wind tunnel data are typically not sufficient, since they are not able to capture the dynamic behavior.

The issue is clearly visible if we consider that the thickness of the membrane at real scale is typically in the range of 1mm. Scaling geometrically such a model to fit within a wind tunnel would imply scaling the thickness proportionally, making the test structure practically impossible to manufacture. Similar effects also manifest for mass and stiffness scaling. Therefore, the large deformations, the dynamic effects, the possible aeroelastic phenomena, resonance events, and all of the consequences emerging from wind-membrane interaction would be missing when using wind tunnel tests due to the rigidity of the scaled-down model. This implies the practical impossibility of constructing similar models hence ruling out physical assessment of the coupled dynamic behavior.

In the last decades, Fluid-Structure Interaction (FSI) techniques have emerged as a potentially effective solution to this problem. FSI approaches essentially combine within a single coupled model both, the structure and the fluid domain, thus relying on the field of Computational Structural Dynamics (CSD) and Computational Fluid Dynamics (CFD).

The actual solution of the FSI problem can be carried out using different approaches, which vary widely in the way the coupling conditions are enforced and as a result in the computational effort needed to reach a result. The interested reader could see [15] for a comprehensive comparison between monolithic and partitioned approaches and [16, 7] as reference works on partitioned FSI formulations.

In the field of wind engineering it is customary to employ "partitioned" approaches in which existing stand-alone computational packages are coordinated to solve the FSI problem (see e.g. [29, 41, 17, 33]).

Restricting the analysis to FSI simulation of lightweight thin-walled structures, it is worth mentioning the work by [20, 34, 1, 18, 42].

In the practice however, due to the stochastic nature of wind, and to the complexity of the computational aspects involved, CFD is not yet as established as CSD in the civil engineering industry. Validation and verification studies are thus mandatory to build the confidence needed to use CFD and FSI approaches in the prediction of wind effects on structures.

Figure 1. uLites project's prototype built in Barcelona, January 2015.

The present work contributes mainly to the purpose of validating and comparing very different CFD methodologies against real measurements. Specifically two of the most-common CFD technologies, Finite Elements and Finite Volumes, are employed in the current work for the simulation of the air flow around the model of an inflatable structure similar to the one shown in Figure 1. Since the current target is to investigate the capabilities of CFD, and with the objective of comparing to wind tunnel data, the model is considered as rigid within the current work. Flexible models were also tested and these will be considered in future publications.

The model employed as a testbed is based upon the output of the European project uLites[1], whose primary objective was the design and construction of a lightweight emergency shelter prototype. Computational simulations using Finite Volume Method (FVM) are carried out with the open-source software OpenFOAM [39]. Finite Element Method (FEM) computations are performed using the open-source Kratos Multi-physics [13, 12].

As a first step of a systematic chain of tests, a uniform and constant air flow is adopted as inlet condition in both the experimental and the computational setup. All simulations are done at the same scale as the wind tunnel to facilitate the comparison with wind tunnel data.

To the knowledge of the authors there are no FEM-FVM comparison in wind engineering CFD problems.

Therefore the objective of this work is twofold. On one hand it provides a reference numerical-experimental benchmark solution of a wind engineering problem using different opensource softwares. This turns out to be an implicit comparison with different numerical techniques such as FEM and FVM. The use of opensource platforms is also an important aspect in view of future reproducibility of the presented results. On the other hand, this case study will serve as a fundamental basis for further investigations considering an Atmospheric Boundary Layer (ABL) flow inlet condition, the real structural scale, the fluid-structure interaction, etc. In the present case study, some essential modeling aspects, typically applied in practice when using the opensource softwares OpenFOAM or Kratos, like e.g. automatic meshing choices, grid resolution, turbulence modeling, and wall functions,

---

[1] Ultra-lightweight structures with integrated photovoltaic solar cells: design, analysis, testing and application to an emergency shelter prototype. EU project within the Seventh Framework Programme, Grant No. 314891 (http://www.cimne.com/websasp/ulites).

are investigated in both packages, reported, compared, and evaluated in light of the available experimental data.

The paper is organized as follows: in section 2 a brief description of the wind tunnel experiment is given. The experimental data are used as a reference in the assessment of the CFD approaches. These are used to assess the performance of the simulations and to estimate the relevance of certain modeling aspects. Section 3 contains an in-depth description of the general computational settings (e.g. computational domain, boundary conditions, etc.) as well as a detailed presentation of the method- and code-specific background (e.g. meshes, numerical schemes, etc.) for FVM/OpenFOAM (section 3.2) and FEM/Kratos (section 3.3). In section 4, the results for each method are systematically presented and compared with the experimental data. A cross comparison between the two distinct CFD approaches is finally performed. Section 5 summarized the main conclusions of the research.

2. **The wind tunnel campaign.** The reference wind tunnel tests were conducted at CRIACIV, a research center for building aero-dynamics and wind engineering located at the University of Florence (Figure 2). The wind tunnel allowed to realize different flow scenarios ranging from a uniform distribution of flow velocities across the wind tunnel section to a fully developed, scaled Atmospheric Boundary Layer (ABL) profile. Both situations were realized within the experimental campaign of the uLites project. However, the scope of this publication is to focus on the case of a uniform flow in order to enable a precise comparison of the two numerical methods considered (FVM and FEM), including the respective modeling choices. Based on these insights, further studies in ABL will be conducted in a subsequent article.

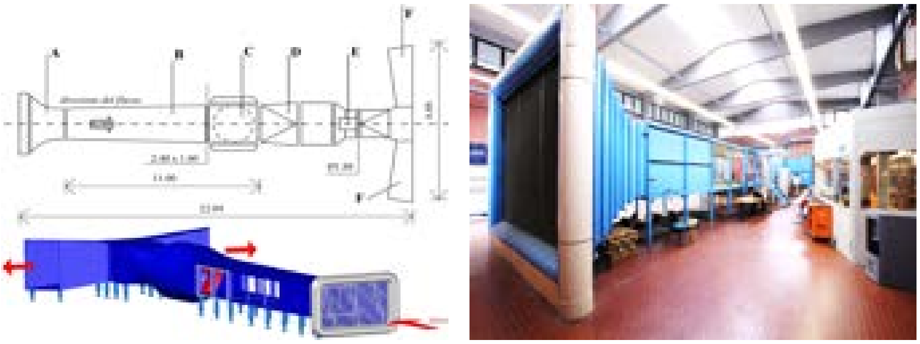

FIGURE 2. CRIACIV wind tunnel and its main components (dimensions are in meters), A: inflow contraction zone, B: boundary layer developing zone, C: test section, D: joint section, E: fan (160 kW), F: T-shaped diffusers [4].

A rigid model of the inflated structure (scale 1:150) was realized by means of rapid prototyping FDM (Fused Deposition Modeling). It consists of four 5cm diameter tubes. The model is 45cm long and 22.5cm high, mounted on a circular base with a diameter of 64cm (Figure 3).

In order to maximize the homogeneity of the steady inlet condition, the model was placed on a wooden table located above the tunnel floor in the vicinity of the centerline of the tunnel. The experimental arrangement is shown in Figure 4. The leading edge of the table had a smooth profile to disturb as less as possible the

Figure 3. Pictures of the shelter model used for the wind tunnel tests.

incoming flow, giving a maximum turbulence intensity not more than 3%. The dimensions of the table were chosen to allow for a suitable wake development. With the previous considerations, a very thin boundary layer was present on the supporting table, allowing the assumption that the floor of the computational domain is a slip surface, and that the inflow velocity is completely uniform. The inflow velocity was chosen to be $u_x = 5.5\text{m/s}$.

For gathering the desired aerodynamic experimental data, a pressure measuring system was employed. The pressure data acquisition system provided simultaneous pressure values on 102 different measuring points distributed over the outer, inner, and side surfaces of the model (Figure 5).

3. Computational setup.

In this work, two numerical methods, each implemented in an open-source software, were used to numerically simulate the wind tunnel tests. Attending to the goal of validating and comparing the two CFD technologies, the modeling efforts focused on achieving as-similar-as-possible simulation setups. However, since the softwares are based on different numerical approaches and discretization schemes both in space and time, an identical configuration for both codes is difficult to be obtained, and some minor differences are inevitably present. In the following, the description of the computational setup is listed starting from the common settings between both approaches (section 3.1), and continuing with each method's specific settings described separately (sections 3.2 and 3.3, respectively).

3.1. Common settings for FVM and FEM simulations.

3.1.1. *Computational domain configuration.* Figure 6 presents the domain configuration used and its associated sizes, as well as the shelter model dimensions. The shelter model representation is positioned with a sufficient surrounding space in order not to be affected by the domain boundary conditions, resulting in an acceptable [21] blockage ratio of $\approx 3\%$. In the downstream direction, a suitable domain length is chosen to ensure that the separation zone is contained within the computational domain. As can be observed, the domain is divided into four different volumes, labeled as Box 0, Box 1, Box 2 and Box 3. This division is conceived to use a different characteristic mesh size for each of the boxes, such that the global computational domain mesh is gradually refined towards the shelter body.

FIGURE 4. Pictures of the experimental setup to realize a uniform inlet profile.

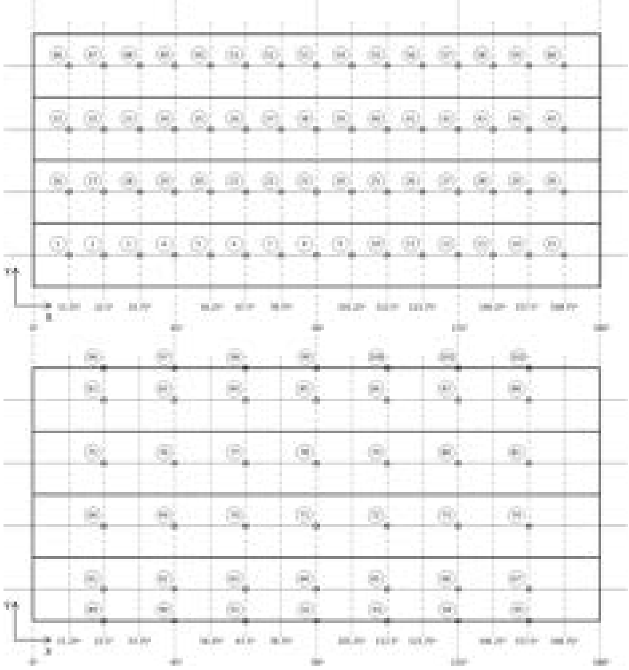

FIGURE 5. Pressure taps on the shelter prototype shown in Figure 1. Outer surface taps ($1-60$ upper figure); Inner ($61-88$) and side surface ($89-102$ lower figure).

3.1.2. *Boundary and initial conditions.* The boundary conditions are defined in the list below, each boundary surface belongs to one of the groups numbered incrementally, as shown in Figure 7.

- Group 1: Inlet boundary:
  - constant and uniform[2] velocity field: $\mathbf{u}[\text{m/s}] = [u_x, u_y, u_z] = [5.5, 0, 0]$,
  - constant and uniform zero pressure gradient: $\frac{\partial p}{\partial \mathbf{n}_x} = 0\text{Pa/m}$.
- Group 2: Outlet boundary:
  - a constant and uniform zero velocity gradient: $\frac{\partial \mathbf{u}}{\partial \mathbf{n}_x}[1/\text{s}] = [0, 0, 0]$,

---

[2] *Constant* denotes time-independent quantities and *uniform* denotes space-independent (spatially homogeneous) quantities.

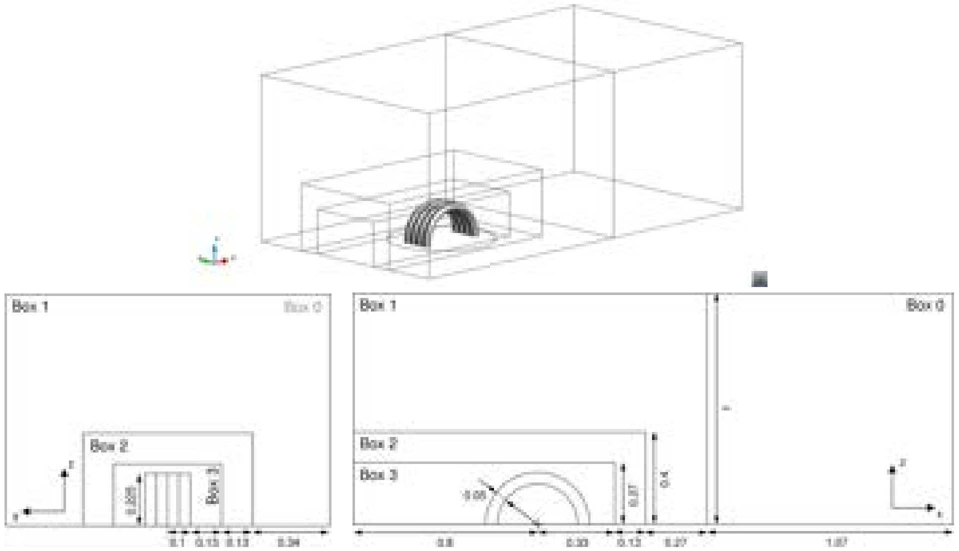

FIGURE 6. Geometry of the computational domain used for the simulations (dimensions are in meters).

  - a constant (zero) and uniform relative pressure: $p = 0\text{Pa}$.
- Group 3: Lateral, top, and bottom walls (including the circular base):
  A slip boundary condition is considered:
  - a constant and uniform boundary-normal component of velocity: $\mathbf{u}[\text{m/s}] = [u_x, 0, 0]$, for the lateral and top/bottom walls respectively,
  - a constant and uniform zero gradient of boundary-parallel components of velocity: $\frac{\partial u_x}{\partial \mathbf{n}_y} = 0$ and $\frac{\partial u_z}{\partial \mathbf{n}_y} = 0$, $\frac{\partial u_x}{\partial \mathbf{n}_z} = 0$ and $\frac{\partial u_y}{\partial \mathbf{n}_z} = 0$ for the lateral and top/bottom walls respectively,
  - a constant and uniform zero pressure gradient: $\frac{\partial p}{\partial \mathbf{n}_y} = 0$, $\frac{\partial p}{\partial \mathbf{n}_z} = 0$ for the lateral and top/bottom walls respectively.
- Group 4: Shelter surface:
  A no-slip boundary condition is applied, imposing a null velocity and pressure gradient on the shelter surface.

As stated in section 2, a slip boundary condition is imposed on the bottom surface since the supporting table is a very smooth surface and thus the thin boundary layer formed can be neglected for the evaluation of pressure coefficients on the obstacle. A comparison to show the significance of this consideration is shown in A.

Regarding the initial conditions, they affect only the initial few time steps of the results. Inlet-equivalent velocity field and outlet-equivalent pressure field, i.e. $\mathbf{u}[\text{m/s}] = [5.5, 0, 0]$ and $p = 0\text{Pa}$, are chosen as an initial solution for the internal fields. The dynamic viscosity of air is assumed to be $\mu = 1.81 \times 10^{-5}\text{Pa} \cdot \text{s}$ and its density $\rho = 1.205\text{kg/m}^3$, which is equivalent to consider a temperature of 20°C.

3.2. **Finite volume method (FVM): OpenFOAM-specific set up.**

3.2.1. *Computational mesh.*

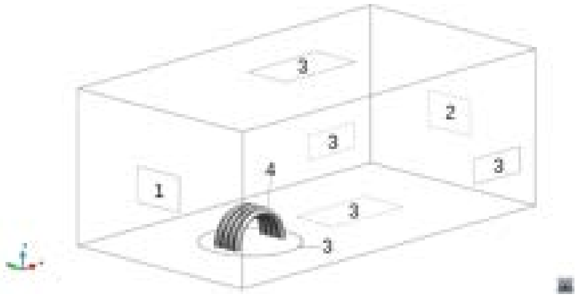

Figure 7. Numbering of the groups of boundary surfaces of the computational domain (1: Inlet, 2: outlet, 3:lateral walls and 4:shelter surface).

- *Mesh type*: the used mesh is a ”modified” structured octree-based mesh unstructured. The elements (the cells) are mainly hexahedra as in classical octree-based medh, with the exception of a 15% of the total number of cells (the cells around the obstacle) which have other polyhedral shapes. *SHM* (*snappyHexMesh*)[3] is the utility used to mesh the domain, to refine at different zones (“boxes” in Figure 6) with the desired refinement level.
- *Mesh resolution control*: some aspects can be crucial when choosing the mesh resolution:
  - According to [21], “In the area of interest, *at least* 10 cells per cube root of the building volume should be used to simulate flow fields.”. Accordingly, $\frac{\sqrt[3]{0.45\times0.2\times0.225}}{10} = 0.0272\,\text{m}$ can be considered as a maximum cell dimension in the area of interest (in our problem, it is the region surrounding the shelter model).
  - Clear representation of the obstacle is needed to assure taking its shape details’ effect into account. Cells with an average dimension of $\approx 2\,\text{mm}$ are used near the shelter model to satisfy its representation.
  - The objective is to design a computational model that will also be usable in the future when the effects of the Atmospheric Boundary Layer flow (ABL wind) on the structure will be modeled. Therefore, Boxes 2 and 3 start at the inlet of the domain to allow a fine enough mesh for the case where an ABL velocity profile will be applied, This would preserve as much as possible the relevant turbulent fluctuations without losing their energy. This procedure is typical in the wind engineering practice for ABL inflow simulations [31, 2][4].
  - Having too fine mesh cells can lead to local amplification of the Courant number, i.e. solution instability, unless a prohibitively small time step is used. In other words, mesh refinement causes significant increase of the computational cost of a desired simulation.

---

[3] *SHM* (*snappyHexMesh*) is a hexahedral-meshing utility in OpenFOAM, designed mainly to catch surfaces, refine surface-neighboring cells, remove the unused cells that the “closed” surfaces contain, and then snap the mesh to them to formulate an obstacle accommodating CFD mesh.

[4] A discussion on the effect of the dimensions of boxes 2 and 3 can be found B.

- *Initial meshing strategy*: the initial mesh is defined considering the previously mentioned criteria while keeping the number of cells at an acceptable minimum, the following approach is adopted: the initial domain is divided into different boxes (Figure 6); starting with cell size: $\frac{1}{15}$x$\frac{1}{15}$x$\frac{1}{15}$ m in Box 0, while Boxes 1,2 and 3 have the first, second, and third levels of refinement, respectively (i.e. $\frac{1}{30}$x$\frac{1}{30}$x$\frac{1}{30}$ m, $\frac{1}{60}$x$\frac{1}{60}$x$\frac{1}{60}$ m, and $\frac{1}{120}$x$\frac{1}{120}$x$\frac{1}{120}$ m). Then, 3 levels of refinement are chosen to reach $\frac{1}{480}$ m $\approx$ 2 mm near the shelter model (Table 1). This approach produces a domain with 550.605 cells, and maximum y^+ (in the expected-detachment region) equals to around 60. We denote this initial mesh as $\mathbf{mesh_0^{OF}}$ (Figure 8).

Box 0	Box 1	Box 2	Box 3	Shelter surface
$\frac{1}{15}$	$\frac{1}{30}$	$\frac{1}{60}$	$\frac{1}{120}$	$\frac{1}{480}$

TABLE 1. Characteristic element sizes for $mesh_0^{OF}$ (dimensions are in meters).

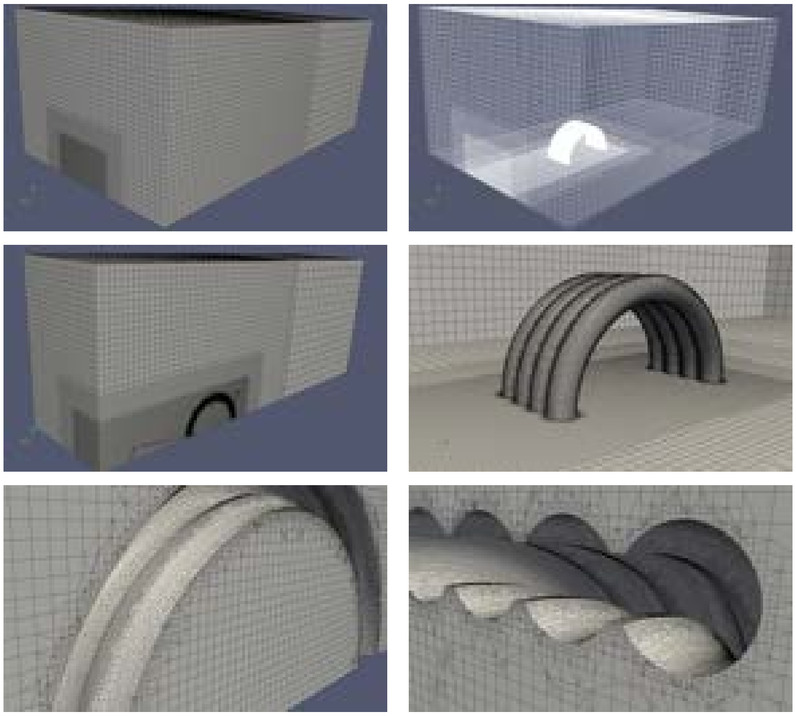

FIGURE 8. Views and sections detailing $mesh_0^{OF}$.

- *Introducing the boundary layer mesh (BL mesh)*: one of the objectives of this study is to test the significance of expensive modeling decisions. One of these is the use of a boundary layer mesh. As a result of the roundness features of the model under investigation, flow separation through boundary layer detachment is expected. Moreover, its exact location is not predictable as in cases with sharp edges. The detection of the separation point, i.e. the point where the forward flow flips backwards and shear stress becomes null, can be of great importance for an accurate prediction of pressure values. To investigate this effect, another mesh ($\mathbf{mesh_1^{OF}}$) is prepared which is $mesh_0^{OF}$ with a BL mesh consisting of 5 layers; starting with the thickness of 3×10^{-4} m next to the shelter model with 1.2 expansion ratio, to result in a BL mesh with a total thickness of 2.2×10^{-3} m. Using the BL mesh results in a 46% increase in the total number of cells to reach a total count of 801 431 cells, and a decrease in maximum y^+ to around 8.

- Increasing the buffer layers between refinement levels: as detailed two points above, 3 levels of refinement were applied on the cells in *Box* 3 to reach the 6^{th} level on the surface of the shelter model. In $mesh_0^{OF}$ & $mesh_1^{OF}$, one buffer layer of cells is applied between different levels to keep the cells count minimum. Keeping in mind the roundness of the shelter model, this sudden change of elements' sizes might disturb the formation of the detached vortices near the structure. To test the significance of this procedure, using *SHM*, 12 buffer layers are added between refinement levels of $mesh_1^{OF}$ to form a new mesh ($\mathbf{mesh_2^{OF}}$). This procedure has increased the number of cells approximately 4 times to reach 3 394 891 cells. Figure 9 shows sections in the three types of meshes.

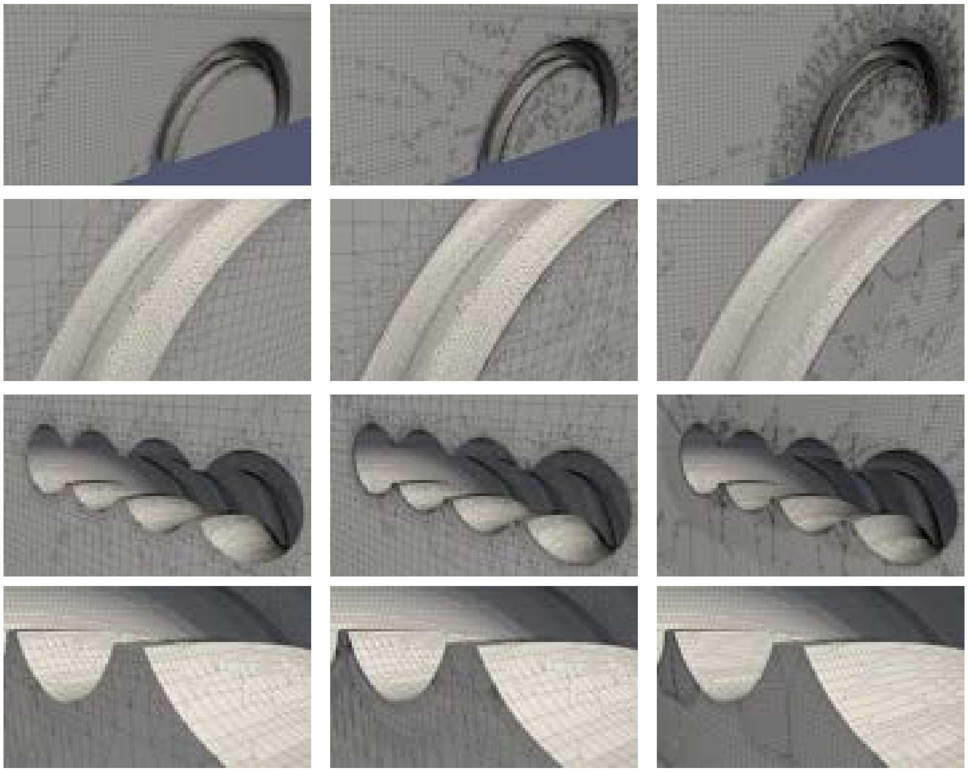

FIGURE 9. Sections showing the evolution from $mesh_0^{OF}$ to $mesh_1^{OF}$ and $mesh_2^{OF}$ (from left to right respectively).

3.2.2. *Numerical schemes.* The truncation error associated with the first order spatial discretization schemes available in OpenFOAM contributes to the solution as artificial-numerical diffusion, causing considerable loss of fluctuations and energy content. Therefore, a second order central difference scheme is used which has been shown to be second order accurate even on unstructured meshes [14], [19].

One drawback of central difference is the tendency towards solution instability due to the unbounded divergence-term discretization, which can be controlled by time step decrement.

Concerning time integration, similarly to spatial discretization, second order schemes should be used to reduce numerical diffusion. The so-called backward difference 2^{nd} order scheme in OpenFOAM takes into account the last two values of the solution variables corresponding to a second-order accurate and implicit scheme. Moreover, the scheme is computationally cheaper than other schemes falling into the same category [14], [25].

3.2.3. *Time step size.* The choice of the suitable time step is critical for managing the overall computational cost. In the simulation scenarios considered here, stability can be the main decisive issue for this choice. To keep the solution stable, especially when unbounded discretization schemes are used, Courant number (CFL) is preferred to be kept small, ideally below 1. The basic relationship is as follows:

$$\Delta t_{\max} = \frac{CFL_{\max} \times \Delta x_{\min}}{u_{\max}} \tag{1}$$

For our unstructured mesh, $\Delta x_{\min}$ cannot be accurately determined. This is also the case for $u_{\max}$. For an initial choice, for $mesh_0^{OF}$, one can use the estimations: $\Delta x_{\min} = 0.002\,\mathrm{m}$, $u_{\max} = 5.5\,\mathrm{m/s}$:

$$\Rightarrow \Delta t_{\max} = \frac{1 \times 0.002}{5.5} = 3.6 \times 10^{-4}\,\mathrm{s} \tag{2}$$

Based on this approximate assessment, a time step size of $\Delta t = 2.5 \times 10^{-4}\,\mathrm{s}$ is used, resulting in a $CFL_{\max} = 1.5$, which is tolerated in our implicit solution approach.

When $mesh_1^{OF}$ or $mesh_2^{OF}$ is used, analogously to $mesh_0^{OF}$ case, one can derive an initial estimation $\Delta t_{\max} = 5.5 \times 10^{-5}\,\mathrm{s}$. Therefore, $\Delta t = 4 \times 10^{-5}\,\mathrm{s}$ is used for the first half a second of the simulation; starting with a $CFL_{\max} = 2$ until reaching a more stable state ($CFL_{\max} = 0.4$) where the velocity field in the BL area converges to small values, resulting in lower CFL number. For the rest of the simulation time, $\Delta t = 2.5 \times 10^{-4}\,\mathrm{s}$ is used again, resulting in a $CFL_{\max} = 2.5$, which is also tolerated in our implicit solution scheme. A comparison to check the validity of this approach is shown in the appendix (Figure 43).

3.2.4. *Turbulence modeling and wall treatment.* In addition to the mesh resolution and design, suitable turbulence closure models and near-wall treatments are further modeling aspects evaluated in this study. To list possible test cases, the following points are taken into consideration:

- Reynolds-Averaged Navier-Stokes (RANS) models typically become less reliable when turbulent unsteady separated flows is achieved. They are more robust and cheap than the Large Eddy Simulation (LES) option to model near-wall flows. Hence they produce good near-wall solutions for relatively coarse and highly anisotropic cells with very large grid spacing in the directions parallel to the wall. A crucial drawback is the temporal-based filtering (averaging) for all scales, causing the inability to preserve time-dependent solutions in the large-scale turbulent main stream, or detached, flow. As a result of this fact, RANS models are becoming less applicable in computational wind engineering applications, where typically the effect of an ABL-flow around bluff bodies needs to be investigated [6].

- Although LES models are known to require structured, fine, and equally spaced meshes in near-wall regions, they have shown good accuracy and efficiency with wind engineering applications without the need of intensive near-wall refinement [22, 30]. This is especially the case of situations where detachment phenomena are less dominant. Even though the shape of the investigated structure in this study has rounded features, LES (k one-equation eddy-viscosity) model still has a chance due to the relatively small y^+ (≈ 60 for $mesh_0^{OF}$). Its performance with a finer mesh ($mesh_1^{OF}$) is also tested to evaluate the effect of driving y^+ to even smaller magnitude (≈ 8) keeping in mind the bad feature that highly anisotropic cells introduce to the LES problem.
- While it is very effective when applying RANS, the use of wall functions in combination with an instantaneous solution technique like LES, as a replacement of fine near-wall cells, is not always a safe remedy. Adhering to a specified velocity profile on the wall might cause an inconsistency between a time-averaged boundary condition and a time-dependent velocity field. This practice can disturb the near-wall turbulence generation cycle which takes place in the region between $y^+ \approx 20$ and $y^+ \approx 60$ [14]. However, it is observed that the use of Werner & Wengle [40] or Spalding [38] wall functions, where an instantaneous correlation between the velocity near the wall and the wall shear stress is assumed, can result in satisfactory results for small y^+ values. Since our cases have a range of y^+ that is relatively small, this procedure is also investigated. Spalding velocity profile (the universal all-y^+ wall function) is used.
- Spalart-Allmaras' Improved Delayed Detached Eddy Simulation (IDDES) technique has proven recently to be a very good compromise to merge RANS's robustness and accuracy in modeling the attached flows, and LES accuracy in simulating the turbulent, separated flows. The initial Detached Eddy Simulation (DES) technique, proposed in 1997 [36], was suffering from the grid induced separation, where the switch between RANS and LES can occur inside the attached boundary layer when an "ambiguous" mesh is used. To form a less mesh-sensitive approach, the delayed version was developed in 2006 making the switch process more sophisticated [37, 24]. An improved version (IDDES) was introduced in 2008 [35] to make DDES free of log-layer mismatch, making it even less mesh-sensitive. This model seems to be very applicable when it comes to high Reynolds-number problems with unstructured meshes when a flow separation is expected. This is the reason why it is also investigated in this study.

3.2.5. *FVM (OpenFOAM) test cases.* Considering the previously detailed computational settings, and to test the performance of each turbulence/wall modeling technique on different meshes, the OpenFOAM test cases are listed in Table 2. The first and last rows are in bold to mark them as main cases. This is done to indicate that the usage of wall treatment is typically a trivial practice when a hybrid approach is adopted, in contrast to a pure usage of LES where near-wall modeling is usually avoided. For each case OF_{ij}, iterating over i would show a comparison between LES and IDDES, while iterating over j would compare the effect of replacing the mesh with a "better" one.

The first two seconds are ignored in the post-processing procedure to avoid the consideration of unphysical quantities accompanying the initiation of the simulation. Two seconds were chosen since it is enough time for a particle to travel much more than the length of the domain at a velocity of 5.5m/s. Due to the nature of the inlet condition (steady velocity field) and due to the small scale of the problem, the convergence of the results is obtained in the first 10 seconds. All the results and comparisons are evaluated considering the time range from 2 to 12 seconds. The wall time needed for the test cases is in the range from 8 to around 20 hours (see Table 3).

	mesh_0^{OF}	mesh_1^{OF}	mesh_2^{OF}
LES	$\mathbf{OF}_{11}$	$\mathbf{OF}_{12}$	$\mathbf{OF}_{13}$
LES+SpWF	OF_{21}	-	-
IDDES-SpWF	OF_{31}	-	-
IDDES	$\mathbf{OF}_{41}$	$\mathbf{OF}_{42}$	$\mathbf{OF}_{43}$

Table 2. OpenFOAM test cases (SpWF stands for Spalding wall function).

Simulation case	Number of cells	Number of processors	Time needed to simulate 12 seconds [hours]
OF_{11}	550.605	16	8.35
OF_{21}	550.605	16	8.14
OF_{31}	550.605	16	10.71
OF_{41}	550.605	16	8.93
OF_{12}	801.431	16	16.85
OF_{42}	801.431	16	19.66
OF_{13}	3.394.891	96	13.82
OF_{43}	3.394.891	96	16.96

Table 3. Time needed to simulate 12 seconds for OF_{ij} test cases.

3.3. **Finite element method: Kratos-particular settings.**

3.3.1. *Computational mesh.* The meshes used for Kratos simulations are fully unstructured, and consist of linear tetrahedral elements. Although the use of hexahedra, or even of higher-order elements is straightforward in the context of the finite element method, the choice of tetrahedral elements is made so to allow a fully automatic mesh generation. This of course implies some trade-off between the computational accuracy that could be achieved for a given number of degrees of freedom and the ease/robustness attainable when automatically generating tetrahedral meshes.

On the Kratos side, GiD (`https://www.gidsimulation.com/`) is the software used for preparing the geometry and meshing the computational domain. In this case, the meshing procedure is based on an advancing front technique. In a similar fashion to what is detailed in section 3.2.1, three different meshing strategies have also been devised for Kratos cases, namely:

- The initial (or simple) mesh (denoted for Kratos as $mesh_0^K$): this mesh uses the characteristic element sizes given by the initial meshing strategy of $mesh_0^{OF}$. Each box has a different element size, decreasing with a factor of 2 towards the structure surface. The different values are summarized in Table 1.

  In order to minimize the resulting number of elements, the transitions on element size between the different regions are made as fast as possible. In GiD, this is controlled by a parameter that ranges between 0 (slowest transitions) and 1 (fastest transitions). For this mesh case, a value of 1 is selected.

  This configuration produces a mesh with 3 957 112 elements, which is illustrated in Figure 10 (to be directly compared with Figure 8 for the OpenFOAM case). The volume ratio between a regular hexahedron (cube) and a regular tetrahedron is shown to be $6\sqrt{2} \approx 8.5$, so recalling that $mesh_0^{OF}$ has 550.605 cells, the expected number of elements for $mesh_0^K$ is about $550\,605 \times 8.5 \approx 4\,680\,142$, which is comparable to the actual value obtained. As before, the resulting y^+ value for this mesh configuration is approximately 60.

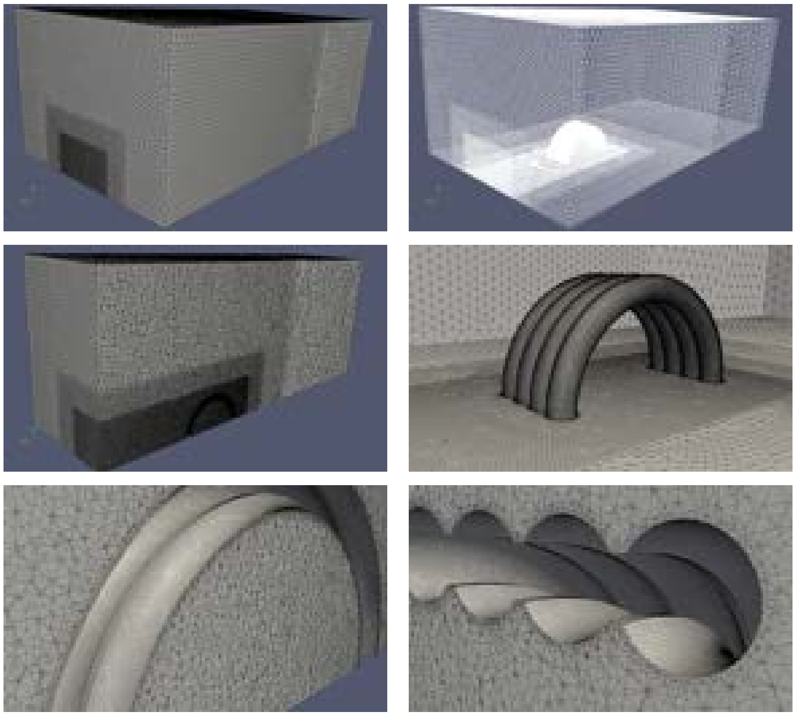

FIGURE 10. Views and cuts detailing $mesh_0^K$.

- The initial strategy plus a boundary layer (BL) mesh on the shelter surface (denoted for Kratos as $mesh_1^K$): as discussed in section 3.2.1, given the importance of mesh resolution in the flow separation region, a BL mesh is also introduced in the initial Kratos setup. This is also a tetrahedral mesh which, as in the OpenFOAM case, consists of 5 layers that grow progressively in size with a factor of 1.2. The first layer thickness (mesh height in the shelter surface) is also 3×10^{-4} m, resulting in a total BL mesh height of 2.2×10^{-3} m. Once again, this configuration is homologous to $mesh_1^{OF}$. Like before, the size transitions between the different boxes are made as fast as possible.

As noted previously, the addition of a boundary layer mesh implies an important increase in the number of elements. Actually, with this configuration GiD produces a mesh of 6 529 478 elements, which again follows the equivalence rule with OpenFOAM reasonably well ($801\,431 \times 8.5 \approx 6\,812\,163$). To illustrate the BL mesh in Kratos, Figure 11 includes different cuts of $mesh_1^K$ in the region near the shelter surface (comparable to Figure 9 for the OpenFOAM case).

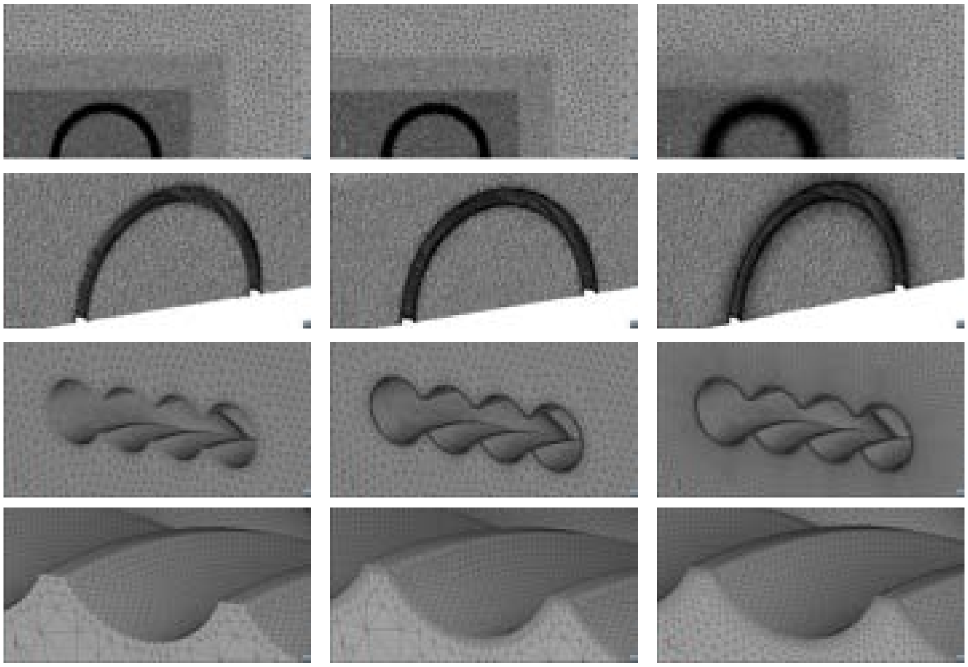

FIGURE 11. Cuts showing the evolution from $mesh_0^K$ to $mesh_1^K$ and $mesh_2^K$ (from left to right respectively).

- Smooth-transition meshing strategy (labeled as $mesh_2^K$): sudden size transitions between elements can have a negative influence in the solution of the flow detachment region in the vicinity of the structure (see section 3.2.1). To analyze this effect, and following a similar philosophy as in $mesh_2^{OF}$, the element size transitions between the different regions are made smoother in this case. Hence, this third strategy takes the same configuration used in $mesh_1^K$ but with the size transitions GiD control parameter decreasing down to 0.1. This produces very smooth transitions, causing the number of elements in the mesh to largely increase up to 8 980 155. The details of this mesh near the body are also displayed in Figure 11, which can be directly compared with the other meshes.

3.3.2. *Numerical schemes.* In the context of the finite element method, it is well known that the application of the Galerkin method to the discretization of convection-dominated problems leads to uncontrolled oscillations in the spatial solution. Moreover, the saddle point nature of the problem to be solved, lead to an additional constraint in the choice of the velocity and pressure finite element spaces in order to fulfill the *inf-sup* or LBB condition. For instance, the classical and widely used choice of equal order spaces for velocity and pressure does not comply with the LBB condition and lead to unstable solutions. To a large extent, these problems caused the delay in the application of the FEM with respect to the FVM in the realm of CFD.

Techniques to circumvent such limitations were introduced during the second half of the 90s, thanks in particular to the seminal work of Hughes and others [26, 27, 28]. The variational multiscale (VMS) approach represents a modern version of such early techniques.

The idea at the basis of the VMS method is actually rather simple. The real solution $\mathbf{u}$, p is seen as the sum of its finite element counterpart (also called large scale), $\mathbf{u}_h$ and p_h, plus the unresolved scale, i.e. $\mathbf{u}_s$ and p_s, also known as the subscale (or small scale). The deriviation of a classical Galerkin weak form bring to a residual-based stabilized formulation. Such splitting have to be also applied to the velocity and pressure test functions (which live in the same space than velocity and pressure, respectively) Further details can be found for instance in references [10, 11].

In other words, the VMS technique can be viewed as a means of stabilizing the central finite element discretization provided by the Galerkin method.

Despite the wide difference in the mathematical reasoning, the splitting at the base of the VMS is obviously similar to that of the LES method. The advantage of the VMS over other alternatives is that the Galerkin approach provides a consistent way of applying the stabilization model on the top of any finite element discretization, independently of the topology chosen and of the skewness of the elements. This in turn makes the FEM-VMS approach very robust against mesh skewness and very flexible in the choice of the discretization to be employed.

Kratos relies on the previous formulation to spatially discretize the computational fluid domain, which is combined with a second-order, implicit, backward differencing scheme for time integration.

3.3.3. *Time step size.* The larger number of elements that is obtained in Kratos meshes results in a higher computational cost than that of the OpenFOAM counterparts. To deal with this increase, given the good stability tolerance of the implicit numerical scheme selected, a larger time step is used. Numerical tests have shown that Kratos cases are able to provide satisfactory results up to a time step of $\Delta t = 0.005$ seconds. Using the same estimations for Δx_{min} and u_{max} as in section 3.2.3, this corresponds to a $CFL_{max} \approx 13.2$. As a trade-off between solution accuracy and computational cost, a fixed value of $\Delta t = 0.001$ seconds is used in all Kratos simulations, giving the reasonable value of $CFL_{max} \approx 2.6$.

3.3.4. *Turbulence modeling and wall treatment.* A recent and very important finding is that the VMS model is sufficiently rich to open a door to the modeling of turbulence. This has been observed independently by many authors over the last years [23, 8, 5, 10]. In particular, it has been proven both theoretically and numerically that FEM-VMS can do direct numerical simulation (DNS), and that for

LES resolutions it has a dissipation structure in accordance with the Kolmogorov cascade [9]. This adds up to the fact that VMS can be fundamentally appropriate to describe the nature of turbulence, with the practical result being that it can be used without any additional turbulence model for the numerical simulation of turbulent flows. Certainly, this provides significant advantages to the numerical solution in terms of complexity and computational cost.

In the finite element approach taken by Kratos, turbulence modeling is directly achieved through the VMS technique used to stabilize the Galerkin discretization, as discussed above.

3.3.5. *FEM (Kratos) test cases.* Four different cases are developed and tested in Kratos. Following a similar listing as in the OpenFOAM section, they are presented in Table 4. The first three cases: K_{11}, K_{12} and K_{13} are purely based on the variational multiscale formulation (3.3.2), and are used to investigate the effect of the boundary layer mesh and the influence of size transitions between elements. On the other hand, the fourth case (K_{21}) incorporates the use of a wall function on the shelter surface, and has the objective of checking if the wall function can provide an accurate solution in the detachment region when using $mesh_0^K$, thus evaluating the need to use a BL mesh for a proper resolution of flow separation. Attending to the previous discussion (see section 3.2.4), the Werner & Wengle wall function model [40] is considered.

	mesh_0^K	mesh_1^K	mesh_2^K
VMS	K_{11}	K_{12}	K_{13}
VMS+W&W	K_{21}	-	-

Table 4. Kratos test cases (W&W stands for the Werner & Wengle wall function).

Following the arguments given in section 3.2.5, and for comparison purposes, the simulation results for Kratos are also post-processed between 2 and 12 seconds. The Kratos wall time needed for each case is given in Table 5.

Simulation case	Number of elements	Number of processors	Time needed to simulate 12 seconds [hours]
K_{11}	3 957 112	192	11.80
K_{12}	6 529 478	192	19.47
K_{13}	8 980 155	192	28.31
K_{21}	3 957 112	192	12.41

Table 5. Time needed to simulate 12 seconds for K_{ij} test cases.

4. **Results and comparison.**

4.1. **FVM (OpenFOAM) results and comparisons.** The following figures attempt to visualize the major flow behavior characteristics for the 6 main **OF** cases.

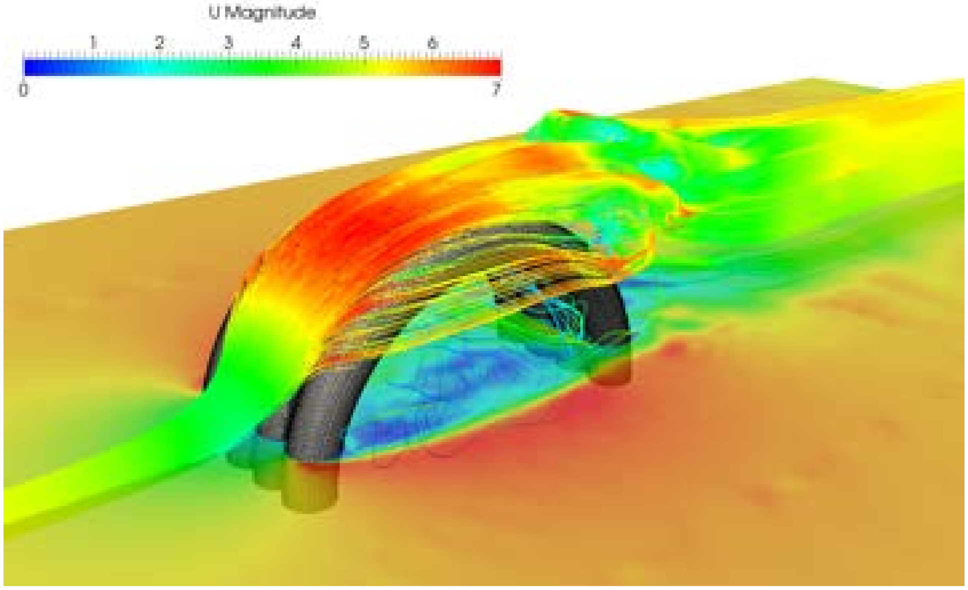

FIGURE 12. Velocity magnitude contours on a horizontal cut plane together with streamlines visualizations.

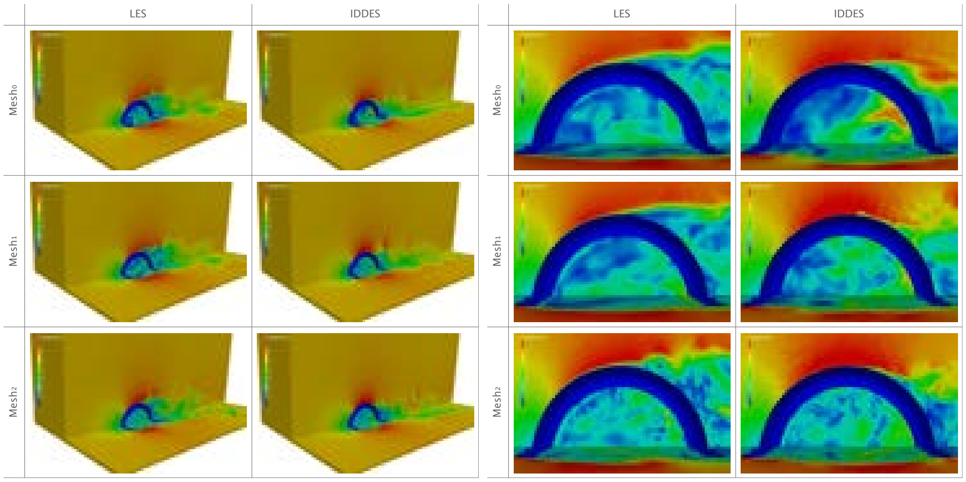

FIGURE 13. Cuts colored by the velocity field at the same time step for different meshes and turbulence treatment techniques (left). A close up view (right).

As previously mentioned, the mesh and turbulence/wall modeling techniques are systematically varied which generates the 8 test cases listed in section 3.2.5. Figure 13 shows velocity contours for the 6 main cases at the same moment in simulation time, while Figure 14 shows them together with the mesh representation. The difference in detachment occurrence between LES and IDDES is clearly observed in those contours: in LES the flow detaches at an earlier location on the outer surface of the shelter. Figure 15 shows the averaged pressure coefficient contours for those cases. To allow for clearer comparison, a sketch (Figure 16) plots averaged C_p diagrams on the pressure taps. Utilizing the problem symmetry, it is enough to plot the output on one middle tube, one side tube, and one set of side taps[5].

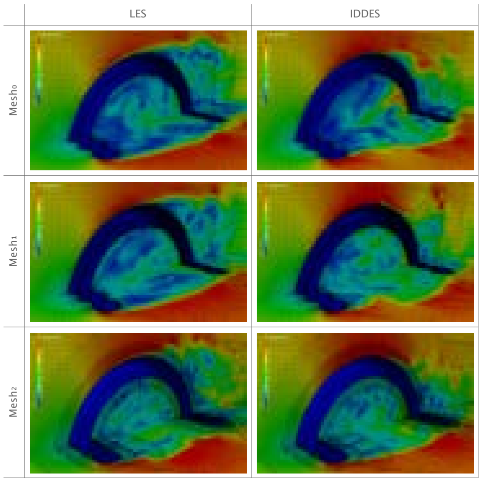

FIGURE 14. Cuts colored by the velocity field for different meshes and turbulence treatment techniques.

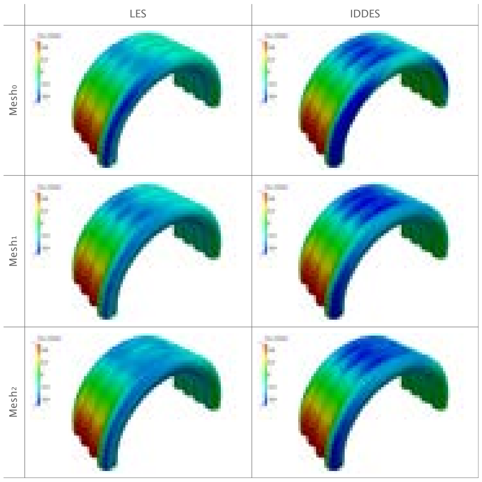

FIGURE 15. C_p averaged field on the shelter for different meshes and turbulence treatment techniques.

Figure 16 shows the cases OF_{11}, and OF_{41}, where the cheapest initial mesh ($mesh_0^{OF}$) is used. It is observed that the LES solution is failing to resolve the detachment zone on the outer surface: it starts to considerably deviate from the reference solution at around 67.5° (taps 6, 21, 36, 51 in Figure 5) and continues to give a wrong prediction for the rest of the structure. IDDES showed a much better performance in handling the detachment zone and beyond. The discrepancy still exists but it is lower than in the LES case.

As previously mentioned, it is trivial to model the near-wall fields when utilizing hybrid approaches within the time-averaged component. Aiming to qualitatively assess the role of the wall function in IDDES, the test case of IDDES was repeated without using the wall function. It showed (Figure 17) a similar behavior as that of the LES case, indicating the significance of the wall function in the time-averaged part of the IDDES. On the other hand, aiming to assessing the role of the time-averaged component of IDDES when a wall model is adopted, and although the instantaneous nature of LES makes the use of a wall function counter-intuitive, another LES test case with Spalding velocity profile (the universal all-y^+ wall function) was carried out, where an instantaneous correlation between the velocity near the wall and the wall shear stress is assumed. Experiences in this field have reported possible bad effects on the boundary layer turbulence generation cycle unless y^+ is

---

[5] Refer to Figures 29 to 39 in the appendix for similar sketches that plot C_p in terms of the standard deviation.

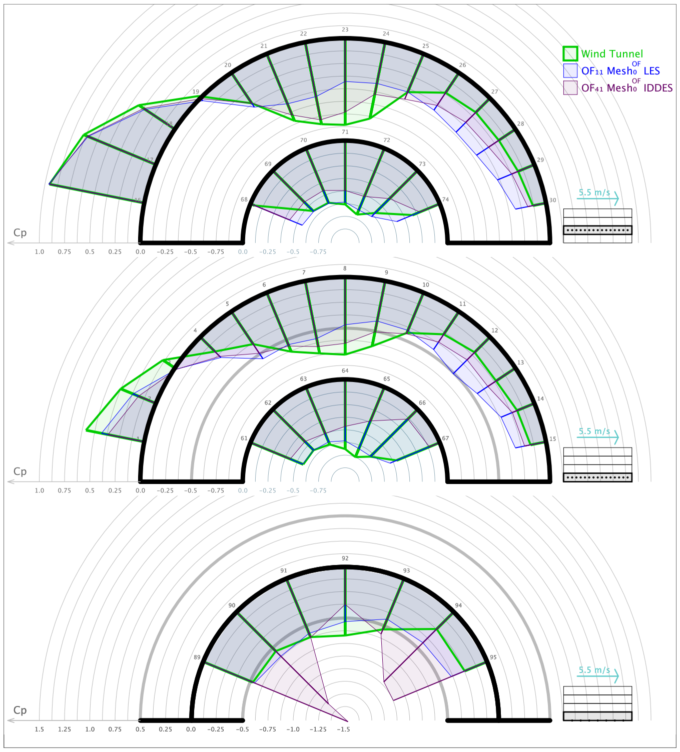

FIGURE 16. Mean of pressure coefficients at the shelter's middle tube, side tube, and on its side using mesh_0^{OF}; once with LES and once with IDDES.

considerably small. The output of this test case is also plotted in Figure 17 showing a graph which is close in shape to the IDDES case but also has a considerable deviation. This experience confirms the effectiveness of the IDDES hybrid approach to handle detachment where the time-averaged model in the boundary layer zone together with the wall function can improve the results considerably without additional computational effort (see Table 3).

The discussion so far shows an advantage of the use of IDDES when compared to LES. However, interestingly, LES on the inner surface and the sides of the structure is doing much better in capturing the correct pressure values using this basic mesh. This fact compromise the possibility to conclude that IDDES is the high-end cheap solution to the turbulence/wall problem, and limits this conclusion to the detachment problem (the outer surface in this case).

From Figures 18 and 19, one observes that the BL mesh (mesh_1^{OF}) has caused LES results at 67.5° to improve. Apart from that, LES continues to fail to resolve the rest of the detachment zone and beyond. On the inner and sides taps, LES reports the same output as when no BL mesh is used (which is already good in mesh_0^{OF}). On the other hand, IDDES shows more advancement on the detachment zone on the outer surface, but with no considerable improvement on the wake side of the outer surface. Interestingly, a considerable improvement is detected on the inner and sides taps; where the results are as good as the LES ones. From this

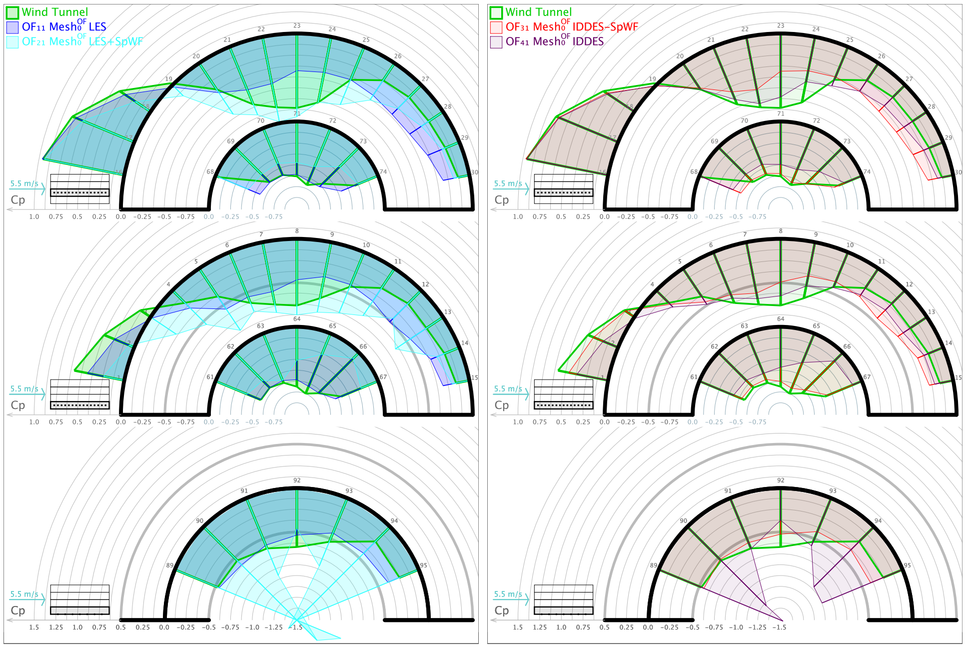

Figure 17. Mean of pressure coefficients at the shelter's middle tube, side tube, and on its side using mesh$_0^{OF}$; "LES" vs. "LES with Spalding wall function" (left) "IDDES" vs. "IDDES without Spalding wall function" (right).

experience one can see the positive effect of having a boundary layer mesh (in this used resolution). While it is not helpful, in the LES solution, to capture the detachment well, this does help the IDDES in resolving the regions where heavy turbulence is to be expected without a clear detachment event.

Increasing the number of buffer layers between refinement regions (i.e. using mesh$_2^{OF}$) was the most rewarding practice. From Figures 18 and 19, one can see the improvement on both solutions. IDDES, in particular, has shown a very good agreement in the wake-facing part of the outer surface. This indicates how refinement helped the vortices that are shedding after the detachment event, to survive in the CFD environment. It also caused IDDES prediction in the inner and side part of the structure to be even closer to the reference solution and to LES. This experience has shown the significance of having a smooth transition between refinement zones. Since *SHM* is a hex-based meshing tool, the only way to have this need fulfilled is by increasing the number of buffer layers between refinement regions.

4.2. **FEM (Kratos) results and comparisons.** Figure 20 presents the results for cases K_{i1}, which are associated to the simple mesh $mesh_0^K$. As can be observed, in both $mesh_0^K$ cases the numerical solution is not capturing the proper physics of the flow in the second half of the outer surface of the shelter, where flow separation takes place. Pressure is considerably underestimated downstream from angle 67.5° until approximately 112.5°, where it starts to become overestimated up to the trailing edge of the structure. Besides, the use of the wall function does not appear to

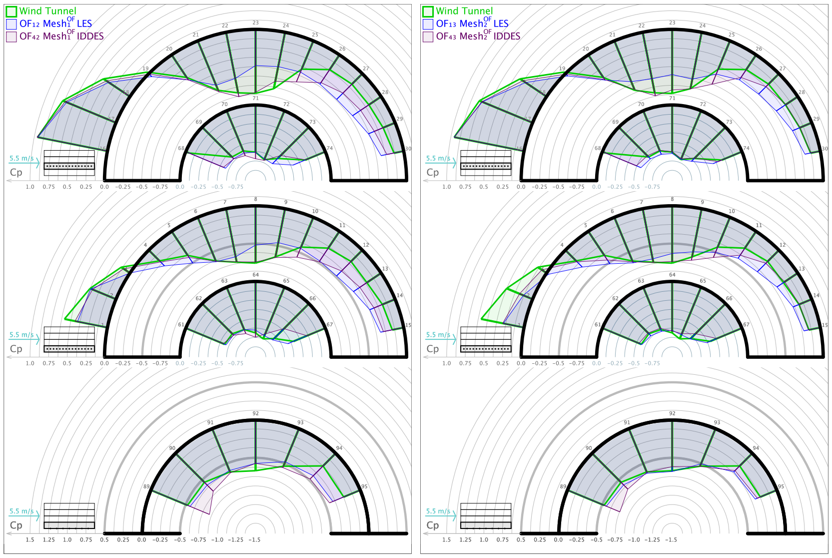

FIGURE 18. Mean of pressure coefficients at the shelter's middle tube, side tube, and on its side for different turbulence treatment techniques using mesh$_1^{OF}$ (on the left), mesh$_2^{OF}$ (on the right).

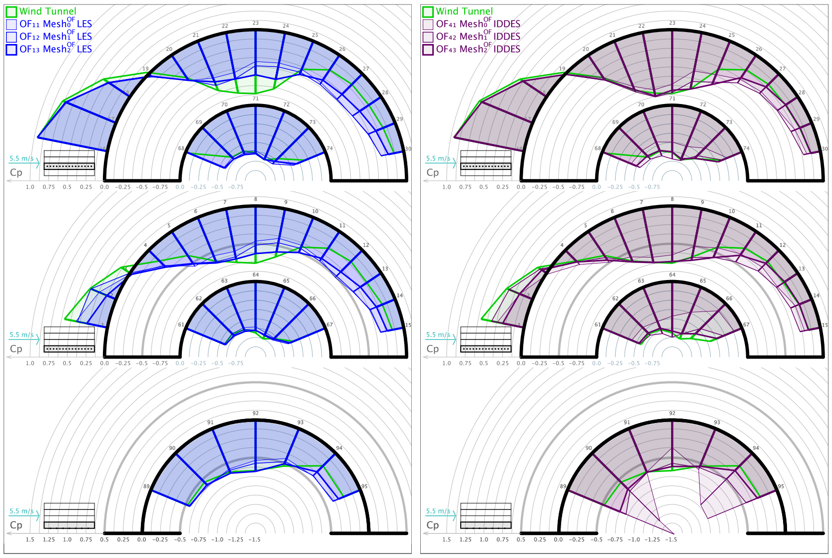

FIGURE 19. Mean of pressure coefficients at the shelter's middle tube, side tube, and on its side for different meshes using LES (on the left), and IDDES (on the right).

bring any clear improvement to the numerical solution. Actually, it is delivering results which are, on average, worse than the ones of the pure VMS case for the initial mesh. The use of the wall law presents a particularly evident side effect: an unexpected error in the predicted stagnation pressure on the center tubes appears.

It can be observed that the behavior encountered in these results is very similar to that found in the OpenFOAM $mesh_0^{OF}$ cases (see Figures 16 and 17). Interestingly,

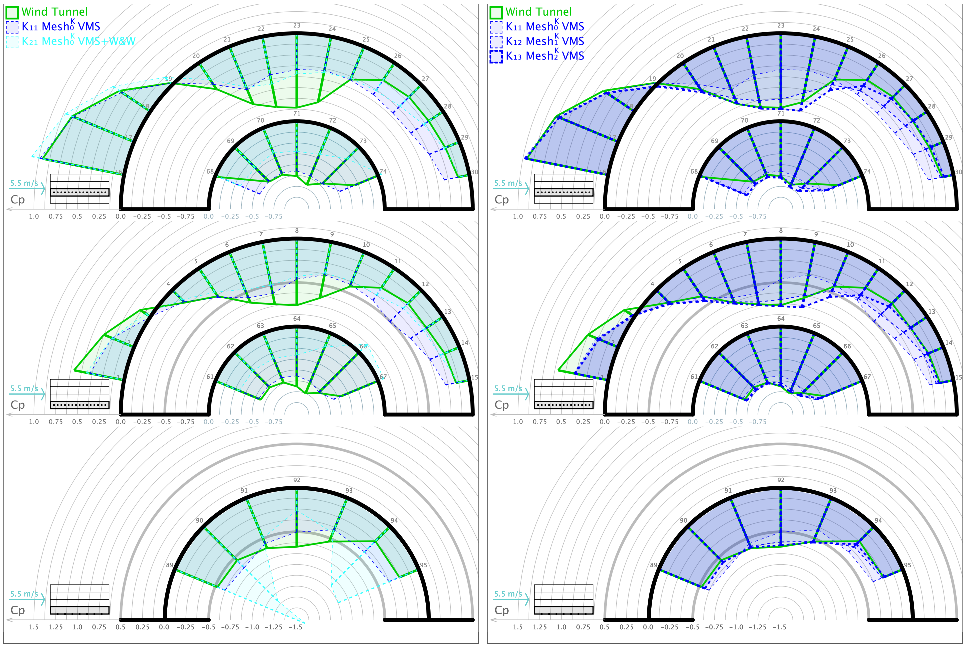

FIGURE 20. Mean of pressure coefficients at the shelter's middle tube, side tube, and on its side for the two Kratos cases using $mesh_0^K$ (on the left) and for the three different Kratos meshes using VMS (on the right).

the VMS results are found to be equivalent to that of LES for the same mesh resolution, and similarly, the case of VMS with a wall function appears to perform in the same way as IDDES at the wake region. For a direct comparison of the results of both codes, refer to section 4.3.

Moving to the other two cases, namely K_{12} and K_{13}, the results are illustrated in Figure 20. As in the case of OpenFOAM, the improvements resulting from the addition of the BL mesh are rapidly noticed. Focusing on the outer surface, the accuracy of the solution in the detachment region is significantly enhanced. In the case of $mesh_1^K$, some deviation is still encountered, especially in the center tubes. However, when smoothing the transitions between elements ($mesh_2^K$), a very good solution is obtained, showing that the flow separation phenomenon is very well resolved. A similar trend is followed in the results at the inner and side taps, where important improvements are also present. The agreement with the experimentally determined reference solution is specially good in the sides of the structure. On the other hand, for the configuration under study the flow inside the shelter is purely due to cross-flow effects and is very turbulent, making the inner region the most complex to predict. This fact can be noticed in the results since the largest deviations are found in the inner pressure taps. Despite this complexity, the inner predictions are reasonably good in these two meshes.

4.3. **FVM and FEM comparison.**

The performance of both codes is compared based on the output of the test cases defined and listed in sections 3.2.5 and 3.3.5.

For clarity, and since we have a couple of factors contributing to this parametric study, the results are discussed distinguishing the position of a tap (either on the outer surface or on the inner/sides surface of the shelter), the mesh, and the turbulence closure modeling methodology. The comparison is summarized in the following Figures, where in Figure 21 the simulations are done using the most basic "cheapest" mesh ($mesh_0$), in Figure 22 using a boundary layer mesh ($mesh_1$) and a boundary layer mesh combined with smoother refinement transition ($mesh_2$). Figure 23 plots the best received output for both codes.

4.3.1. *The outer surface (the detachment problem).*

- **Basic mesh** ($mesh_0$)

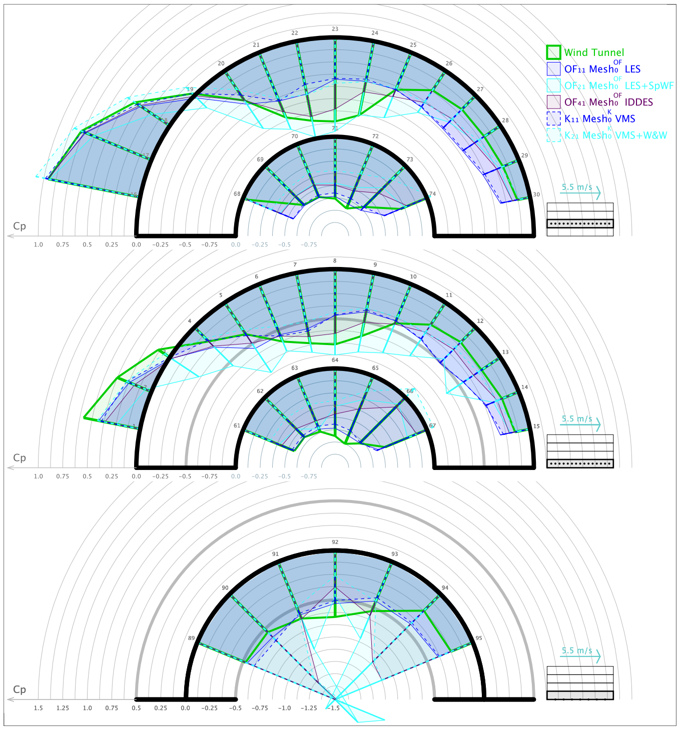

FIGURE 21. Mean of pressure coefficients at the shelter's middle tube, side tube, and on its sides for different CFD technologies and turbulence/wall modeling technique using $mesh_0$ (cases: OF_{i1} & K_{i1}).

Figure 21 shows a very similar performance of FVM-LES & FEM-VMS (almost identical) on $mesh_0$. When a wall function is utilized to improve the results while keeping the cost (element count) to a minimum, even though an improvement on the wake side of the outer surface on both methods is observed, the resolution of the detachment event is not properly achieved, with a difference: where OpenFOAM overestimates the negative pressure and Kratos underestimates it. On the other hand, the hybrid FVM-IDDES showed the best performance on $mesh_0$ with regards to the outer surface, proving its potential as a cheap alternative when it comes to detached flows problems.

- **Boundary layer mesh** ($mesh_1$)
  Figure 22 shows a clear improvement on FEM-VMS solution when a boundary layer mesh is present. This observation did not apply so clearly on FVM-LES which showed a minimum improvement. Even though VMS is usually compared to FVM-LES in theory, our heuristic observation is that VMS appears to show a better performance in capturing the detachment phenomena. Comparing FEM-VMS with FVM-IDDES for this mesh shows a very similar performance with a couple of minimal discrepancies. This represents a very noteworthy result since no purely physical reasoning at all is used in the design of the VMS technique, i.e. no empirical model constants for an explicitly stated turbulence model are introduced.
- **Boundary layer mesh with smoother refinement transition** ($mesh_2$)
  Figure 22 shows a very good agreement with the experimental results when $mesh_2$ is used. The major improvement is observed on the wake part of the outer surface, implying the significance of smooth mesh refinement and its role in resolving the obstacle-induced vortices. Again, FVM-LES improvements were not as good as those of FVM-IDDES & FEM-VMS which were, for the most part, very similar. For clarity, Figure 23 plots the "best" output of both codes on the outer surface, i.e. VMS from Kratos & IDDES from OpenFOAM.

4.3.2. *The inner surface & sides taps (the turbulent flow problem).*

- **Basic mesh** ($mesh_0$)
  As shown in Figure 21, FVM-LES & FEM-VMS perform more or less the same, with FVM-LES doing a bit better at some taps. Interestingly, the results are in a very good agreement with the reference solution even when using the "cheapest" mesh. On the other hand, the hybrid FVM-IDDES, FVM-LES with a wall function, and FEM-VMS with a wall function showed a very considerable deviation from the reference solution when $mesh_0$ is used. This brings up an interesting conclusion that an approach that includes a type of field averaging like IDDES, or the employment of a wall function can be destructive when a very turbulent flow is to be expected with a considerable value of y^+. This behavior was also mentioned in [3, 32, 14], where DES was considered as "inherently unsuited" to cases where the flow is dominated and/or strongly affected by wall-attached eddies. Adapting a plain FVM-LES or FEM-VMS in such cases will give a much better output. One should note here that the pressure coefficient at tap 68 is reported by the wind tunnel engineers to be very small (almost zero)[6]. This small value was not achieved using any (even the finest) of the CFD simulations reported in this paper, suggesting the possibility of tap 68 being defect in the experiment.
- **Boundary layer mesh** ($mesh_1$)
  As shown in Figure 22, the boundary layer mesh improved the results of all three solutions. In particular, FVM-IDDES showed a considerable improvement in pressure values prediction, but did not perform as good as FVM-LES or FEM-VMS.
- **Boundary layer mesh with smoother refinement transition** ($mesh_2$)
  The same previous observation applies in this case as plotted in Figure 22 showing an overall improvement with FVM-LES & FEM-VMS performing

---

[6] In order to reduce the amount of devices in the wind tunnel, the pressure at tap 75 was taken equal to 68 as a reference based on symmetry.

the best in this case. For clarity, Figure 23 plots the "best" output of both codes on the inner surface & sides taps , i.e. VMS from Kratos & LES from OpenFOAM.

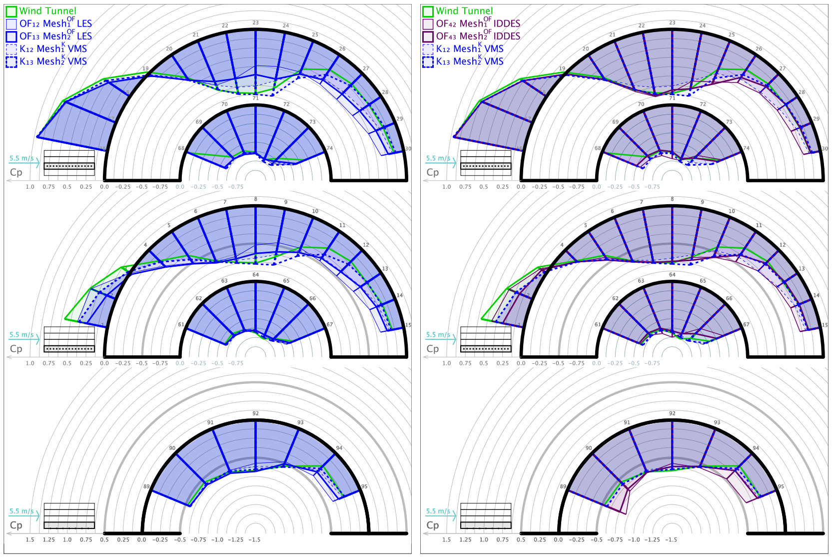

FIGURE 22. Mean of pressure coefficients at the shelter's middle tube, side tube, and on its side for different CFD technologies and meshes (mesh$_1$ & mesh$_2$). Comparing FVM-LES (cases OF$_{1j}$) with FEM-VMS (cases K$_{1j}$) on the left and FVM-IDDES (cases OF$_{4j}$) with FEM-VMS (cases K$_{1j}$) on the right.

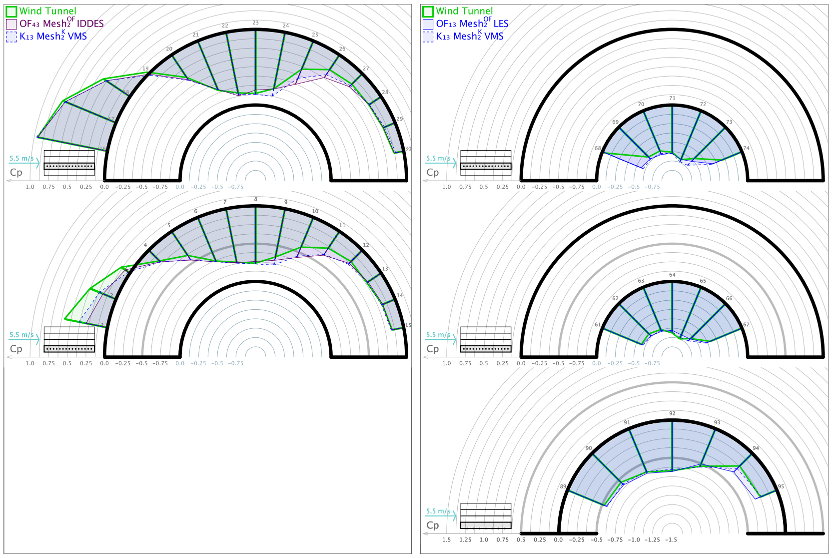

FIGURE 23. Comparing the best output of each CFD technology, namely FVM-IDDES & FEM-VMS on the outer surface, and FVM-LES & FEM-VMS on the inner surface & sides taps.

4.4. **Further observations for other angles of attack.** The wind tunnel experiments also provided the pressure coefficients for other orientations, namely 45° and 90° angles of attack. Following the procedure outlined in the previous sections, CFD simulations for those orientations are performed (Figure 24) and results are compared in Figures (25-28).

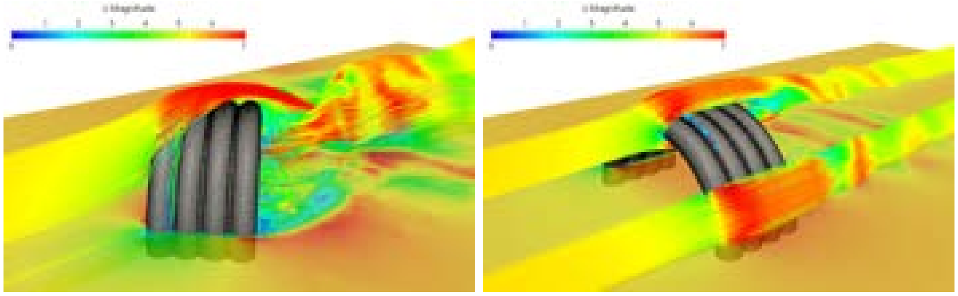

FIGURE 24. Velocity magnitude contours on a horizontal cut plane together with streamlines visualizations for 45° and 90° angles of attack.

In agreement with the discussion previously presented in section 4.3, the following is observed:

- When the basic mesh is used, even though FVM-IDDES is a more sophisticated approach, FVM-LES gives a much more reasonable solution when flow detachment is not dominant. Due to the fact that in 0° orientation the flow detachment dominates the flow behavior on the outer surface, LES with a cheap mesh is considered insufficient. For 45° and 90° angles of attack, this is not the case: the flow separates as soon as it touches the structure due to the small radius of the tube (less "roundness"). This is mostly true in 90° orientation, where the flow in this case behaves more similar to a flow facing a sharp edged body.
- FVM-IDDES does not work for heavily-turbulent flow regions without a boundary layer mesh. In contrast to 0° orientation, for 45° and 90° angles of attack, most of the structure surface faces this type of flow. A boundary layer mesh is essential for IDDES to work properly, while it is not for LES. This observation and the previous one show how an engineer is responsible of choosing the most accurate/cheap approach for each case depending on the structure geometry features and the expected flow behavior.
- On a couple of taps, IDDES combined with a BL mesh is performing better than LES, which is an indicator of a detachment event.
- FEM-VMS shows a performance as good as FVM-LES on the basic mesh, and as good as FVM-IDDES when a boundary layer mesh is used.

5. **Conclusions.**

Analyzing the results of the numerical simulations performed, the following concluding remarks can be extracted.

Focusing on the cases at an angle of attack of zero degrees:

- The initial meshing strategy attempted is not fine enough to resolve the detachment region at the outer portion of the structure. This is specially true

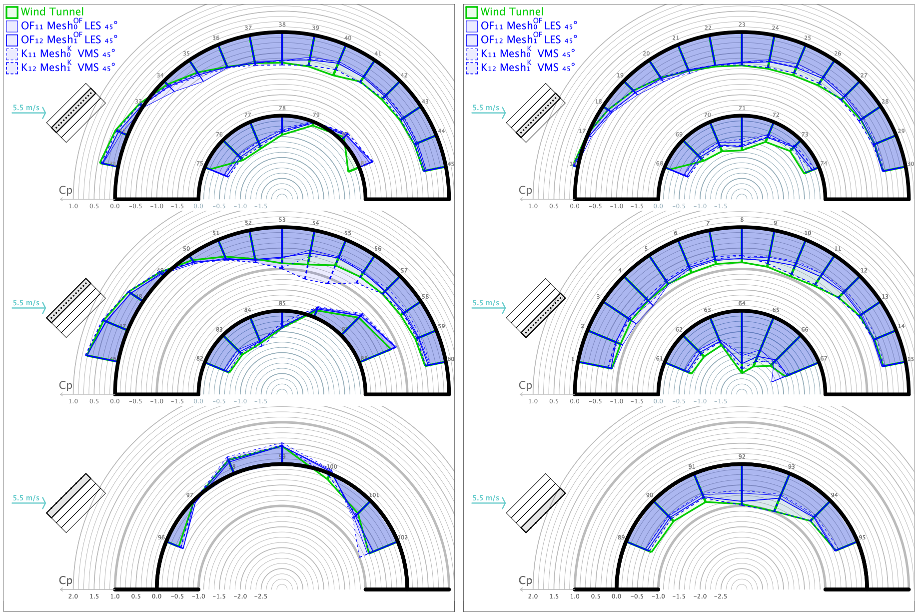

FIGURE 25. FVM-LES vs. FEM-VMS for mesh$_0$ and mesh$_1$ - mean C_p on all taps for 45° orientation.

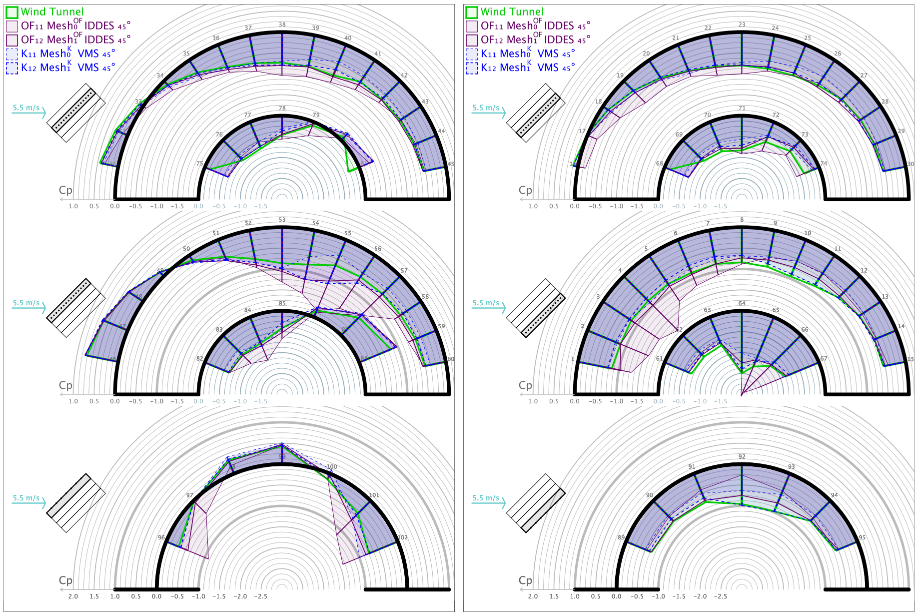

FIGURE 26. FVM-IDDES vs. FEM-VMS for mesh$_0$ and mesh$_1$ - mean C_p on all taps for 45° orientation.

for both the FVM-LES and FEM-VMS approaches, which show very similar results. For the same configuration, the use of FVM-IDDES brings an improvement in the detachment prediction (i.e. the outer surface taps), but it introduces strong deviations in the pressure coefficient at the inner and side taps, something that is not found in the LES and VMS counterparts. The

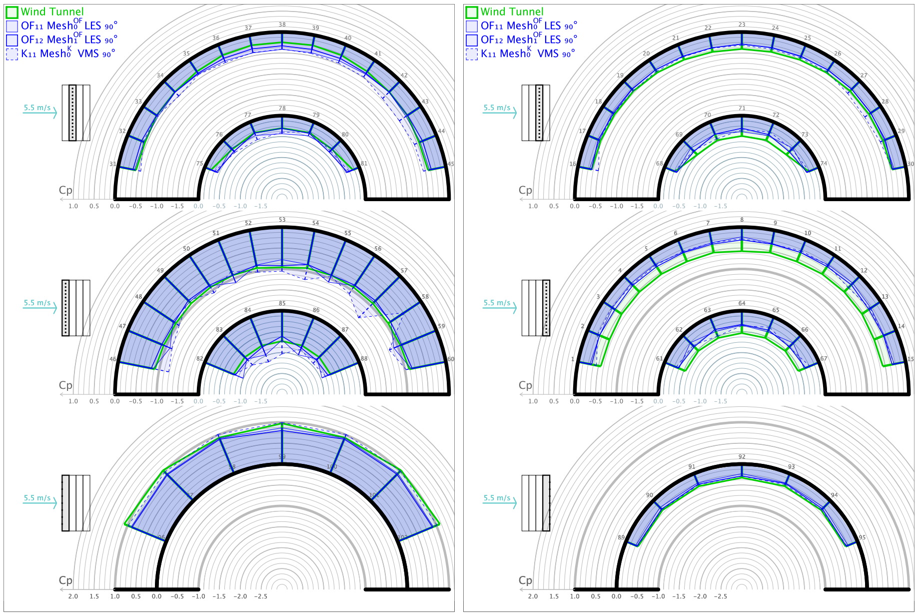

FIGURE 27. FVM-LES vs. FEM-VMS for mesh$_0$ and mesh$_1$ - mean C_p on all taps for 90° orientation.

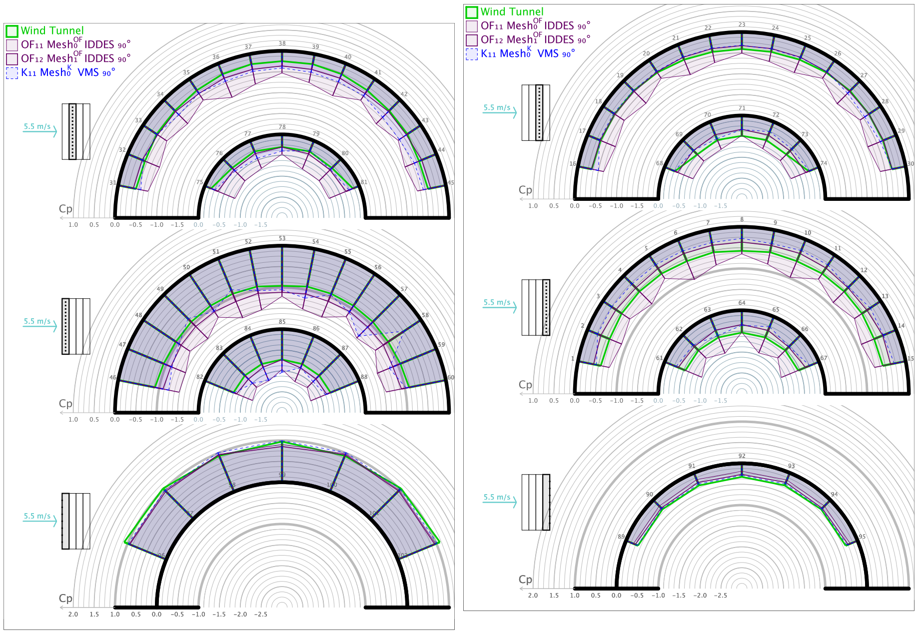

FIGURE 28. FVM-IDDES vs. FEM-VMS for mesh$_0$ and mesh$_1$ - mean C_p on all taps for 90° orientation.

same behavior is found when the Werner & Wengle wall function is used in combination with the VMS method, a result that should be expected since the IDDES technique considered in this study also relies on a wall function

(Spalding model). This observation points out the danger of using a turbulence modeling approach that can disturb highly mixed turbulent flow by introducing a manufactured profile near to the boundary without paying attention to the mesh resolution and y^+ magnitudes.

From these results, it is clear that the initial meshes considered are too coarse to obtain satisfactory solutions manifesting two main challenges:

- a challenge on the outer rounded surface facing the flow: to capture a correct detachment on a curved surface - only IDDES showed an advancement,
- a highly turbulent flow around and "inside" the shelter model where LES & VMS showed a better performance than IDDES.

When attempting to improve the performance of both LES & VMS by a wall function on the outer surface, improvements were not attained.

- Considering the detachment challenge, when the boundary layer mesh is used, the numerical quality of IDDES & VMS solutions is considerably improved. The best results are delivered by these two when smoother refinement transition was applied in the region surrounding the model geometry leading to a very close agreement with the reference solution on the back side of the shelter; an improvement that was not attained through the boundary layer mesh alone. This reflects the need of the higher mesh resolution surrounding the model in order to resolve the detached vortices. LES performance improvement with better meshes was insignificant compared to the other two methods. Not the boundary layer mesh nor the higher surrounding mesh resolution could help LES to improve on the detachment region.

  Considering the highly turbulent flow regions (i.e. inner side of the shelter and on the side taps, where strong vorticity occurs in the recirculation zones), IDDES showed a significant improvement in its output to an acceptable level when a boundary layer mesh is used; showing the power of the hybrid RANS/LES performance where RANS models the near-wall part cheaply via the highly anisotropic, and thus cost-effective, FV cells. This realization encourages relying on IDDES if the mesh is well-designed.

- Overall, the results show an important advantage of IDDES in front of LES for the problem under consideration, where IDDES is able to provide more accurate solutions at the expense of a moderate increase in the computational cost. Similarly, VMS also shows a superior performance than LES in this study, being able to resolve the flow detachment with a better accuracy. Although LES and VMS are fundamentally similar, the robustness provided by the VMS technique in the regions of large element skewness, such as the boundary layer mesh, appears to play an important role in the solutions performed, ultimately leading to a better quality when VMS is considered.

- An important observation about VMS is the ability to perform as good as LES in the initial mesh (on the inner shelter surface and on the sides), and as good as IDDES (on the outer shelter surface) when a boundary layer mesh is introduced. This is consistent with the arguments given before regarding the good flexibility and robustness of the VMS approach with respect to mesh topology and skewness. It is important to emphasize that this conclusion is based on a couple of modeling assumptions discussed in section 3, one of which is the decision regarding the similarity between a tetrahedral mesh and a hexahedral one. It was accepted that each hexahedron is to be compensated by approx. 8.5 tetrahedron to account for the "same characteristic element size", resulting in a larger mesh on the VMS side. This comes with a considerable computational cost compared to the FVM model. A similar discussion applies also for the temporal resolution where in VMS considerably larger time steps can be used without affecting the solution's stability and accuracy. Therefore, a deeper investigation to gauge the comparability in spatial and temporal resolutions between the two CFD methods is of interest.

Regarding the simulations for the other angles of attack, namely 45 and 90 degrees, the results show similar trends as those already discussed. Nevertheless, in these cases, the flow detachment regions are smaller, and LES is able to provide better results than for the 0 degrees case. This observation enforces the conclusion that the sharper the edges are, the more reliable LES can be in computational wind engineering without the absolute need for the hybrid approach.

These insights on how mesh resolution & mesh design on one side, and turbulence modeling techniques & wall treatment on the other, affect each other's impact on the simulation output emphasizes the importance of such modeling decisions. It is also noted that the structure geometrical shape and the expected flow behavior should be considered concurrently. The experiences of this study will support the definition of suitable numerical models for similar CWE simulations setups.

Concluding on the capabilities of FVM and FEM, and also the codes used in this study, the results achieved with both software are satisfactory and share many similarities, demonstrating the capability of both approaches to obtain realistic results on complex structures.

6. Code sharing.

All the developed models have been simulated using two open source platforms that can be downloaded in their latest version from these pages:

- KRATOS multiphisics is distributed under the BSD4 licence, web page: https://kratosmultiphysics.github.io/Kratos/ , source code downloadable at: https://github.com/KratosMultiphysics/Kratos, GUI available at: https://github.com/KratosMultiphysics/GiDInterface.
- OpenFOAM is distributed under the GPLv3 licence: web page: https://openfoam.org/, downloadable at: https://openfoam.org/download/

Acknowledgments. The authors gratefully acknowledge the support of the Institute of Advanced Studies of the Technical University of Munich through the Hans Fischer Fellowship program as well as the support of GNCS by Indam. The authors also acknowledge financial support from the Spanish Ministry of Economy and Competitiveness, through the "Severo Ochoa Programme for Centres of Excellence in R&D" (CEX2018-000797-S). The authors would like also to thank Dr.-Ing. Alexander Michalski from SL-Rasch GmbH for the provided support. The experimental work has been performed by CRIACIV at the University of Florence under the supervision of Prof. Gianni Bartoli.

Appendix A. Comparing the standard deviation of C_p.

When dealing with membrane structures,in addition to the presented mean C_p values, the transient component of the pressure fields is also significant. For this reason, in this section, the results in terms of standard deviation are shown. Observing Figures 29 to 39 it is evident that similar observations made on averaged C_p are also valid for the standard deviation values. Besides, an increment in the deviation of C_p (in the range 0.06-0.08) on the inlet-facing part of the outer side of the structure. This difference is explained by the unavoidable turbulence that occurred in the wind tunnel. Namely, a turbulence intensity of about 3% is measured along the height of the wind tunnel section in the longitudinal direction. It is worth mentioning that this additional turbulence is not considered in the simulations as the inlet flow is set to be uniform and constant.

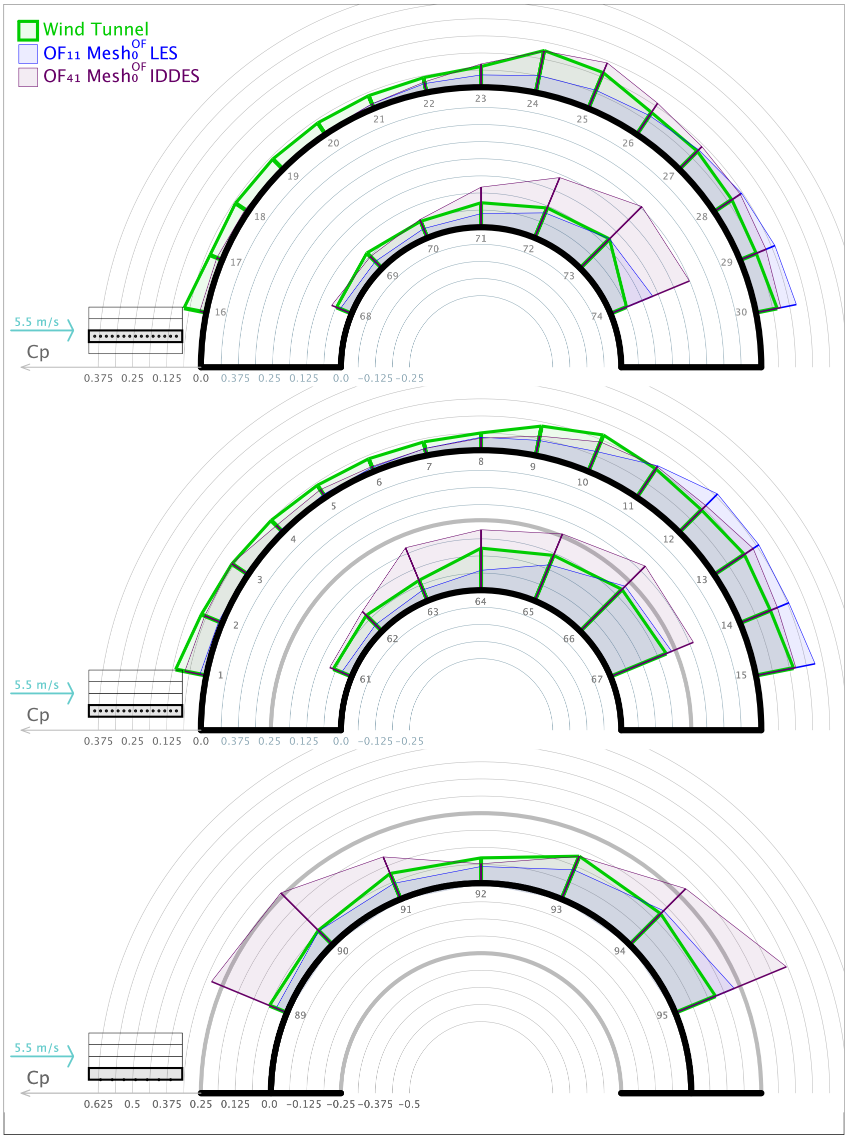

FIGURE 29. Standard deviation of pressure coefficients at the shelter's middle tube, side tube, and on its side using mesh_0^{OF}; once with LES and once with IDDES [refer to Figure 16 for mean values].

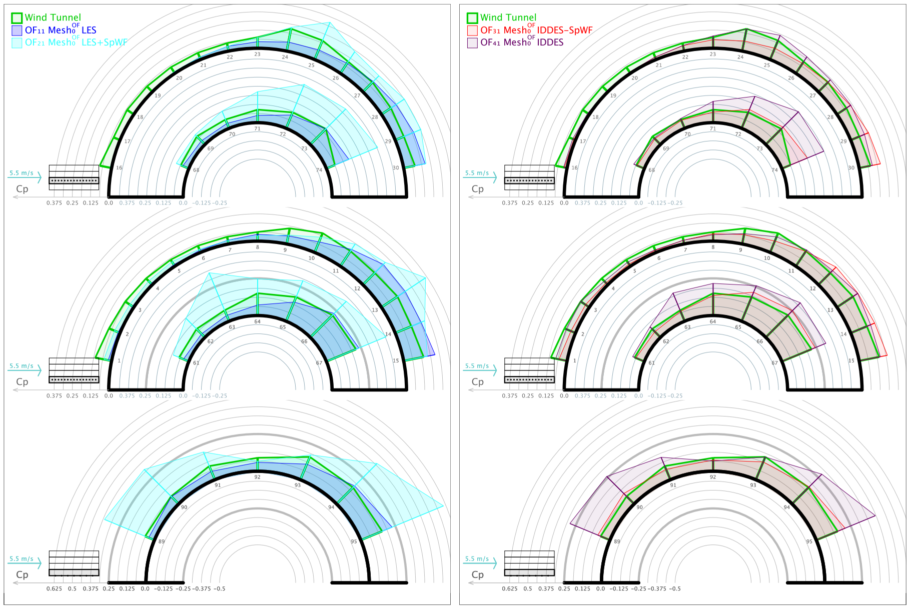

FIGURE 30. Standard deviation of pressure coefficients at the shelter's middle tube, side tube, and on its side using mesh$_0^{OF}$; "LES" vs. "LES with Spalding wall function" (left) "IDDES" vs. "IDDES without Spalding wall function" (right) [refer to Figure 17 for mean values].

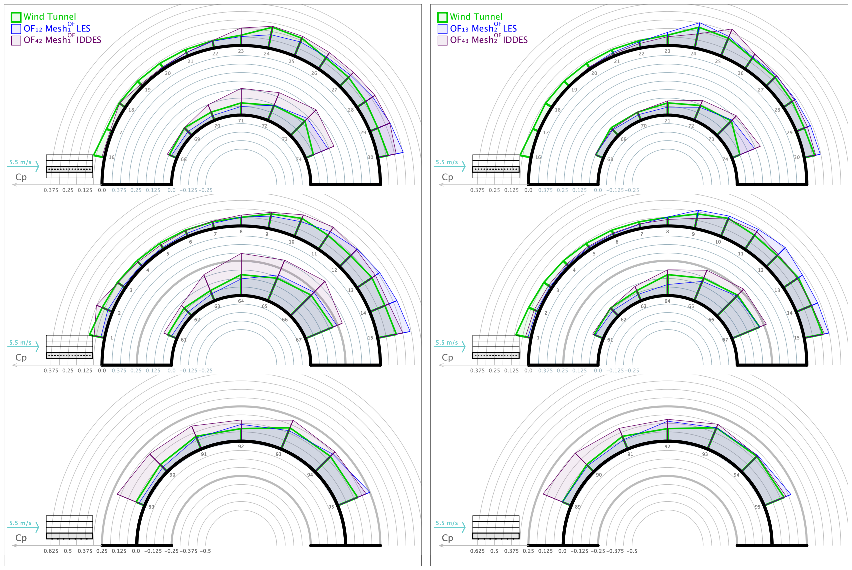

FIGURE 31. Standard deviation of pressure coefficients at the shelter's middle tube, side tube, and on its side for different turbulence treatment techniques using mesh$_1^{OF}$ (on the left), mesh$_2^{OF}$ (on the right) [refer to Figure 18 for mean values].

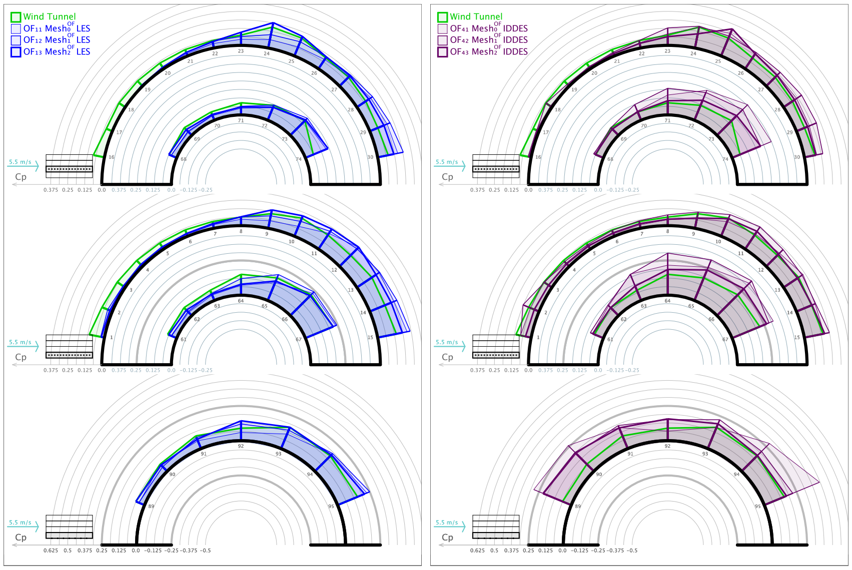

FIGURE 32. Standard deviation of pressure coefficients at the shelter's middle tube, side tube, and on its side for different meshes using LES (on the left), and IDDES (on the right) [refer to Figure 19 for mean values].

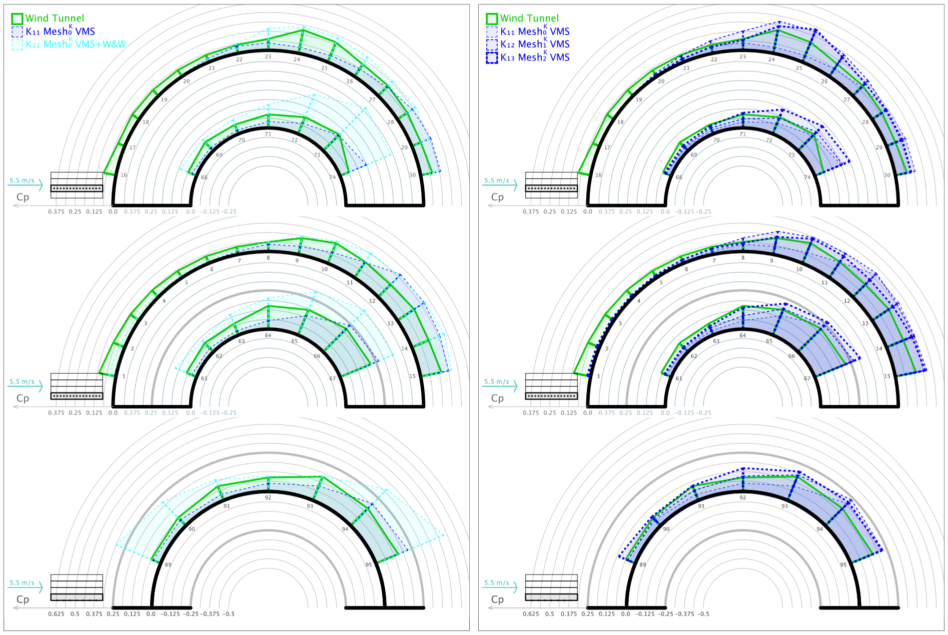

FIGURE 33. Standard deviation of pressure coefficients at the shelter's middle tube, side tube, and on its side for the two Kratos cases using $mesh_0^K$ (on the left) and for the three different Kratos meshes using VMS (on the right) [refer to Figure 20 for mean values].

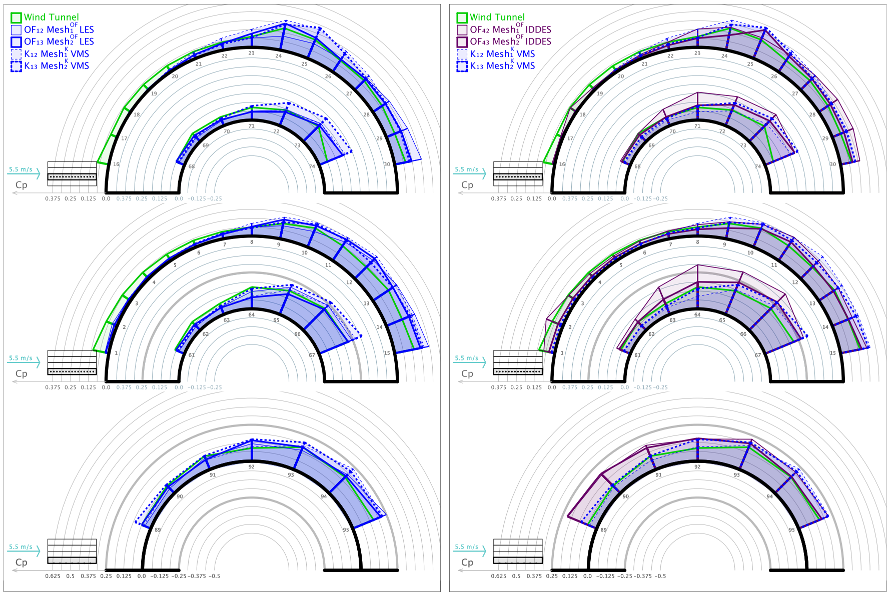

FIGURE 34. Standard deviation of pressure coefficients at the shelter's middle tube, side tube, and on its side for different CFD technologies and meshes (mesh$_1$ & mesh$_2$). Comparing FVM-LES (cases OF$_{1j}$) with FEM-VMS (cases K$_{1j}$) on the left and FVM-IDDES (cases OF$_{4j}$) with FEM-VMS (cases K$_{1j}$) on the right [refer to Figure 22 for mean values].

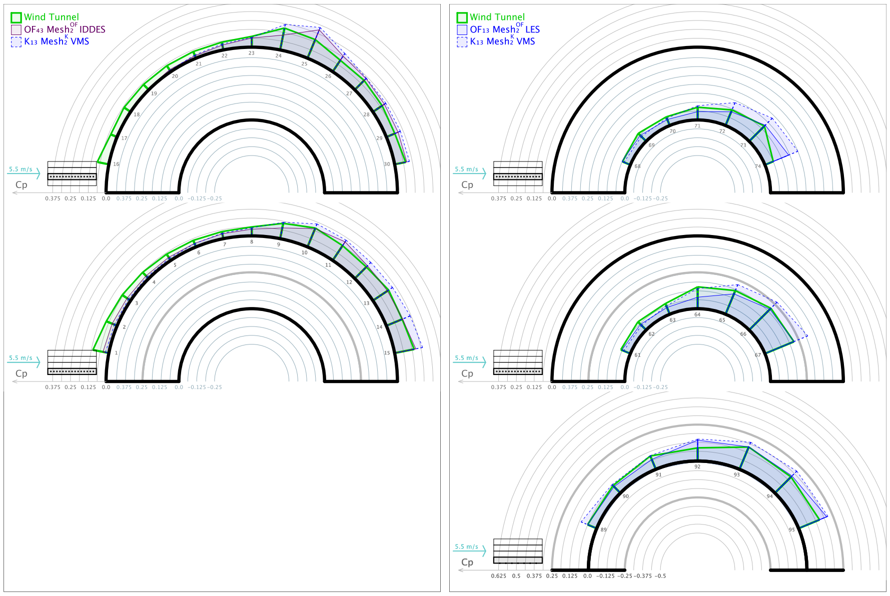

FIGURE 35. Comparing the best output of each CFD technology (in terms of standard deviation of C_p), namely FVM-IDDES & FEM-VMS on the outer surface, and FVM-LES & FEM-VMS on the inner surface & sides taps [refer to Figure 23 for mean values].

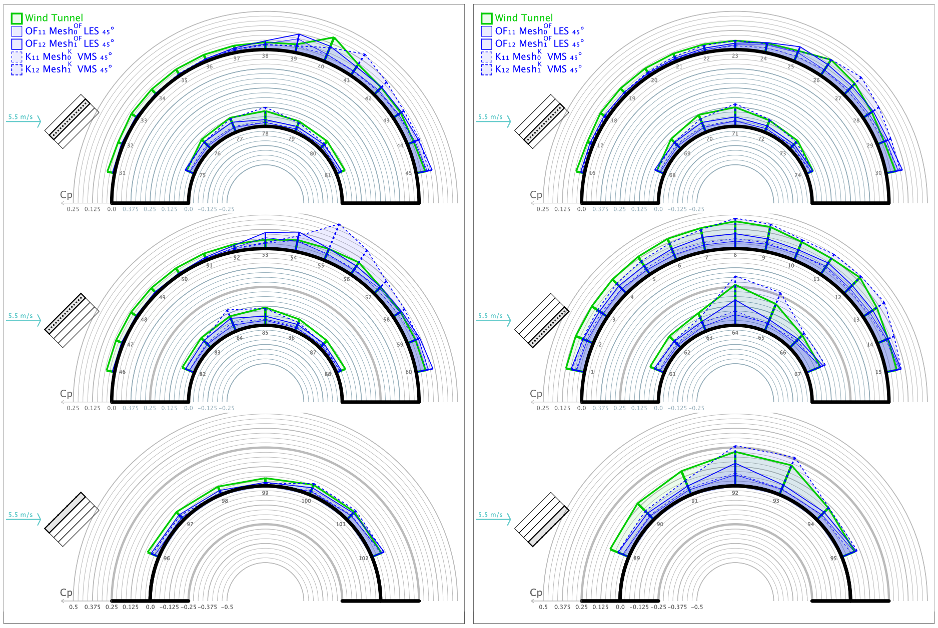

FIGURE 36. FVM-LES vs. FEM-VMS for mesh$_0$ and mesh$_1$ - standard deviation of C_p on all taps for 45° orientation [refer to Figure 25 for mean values].

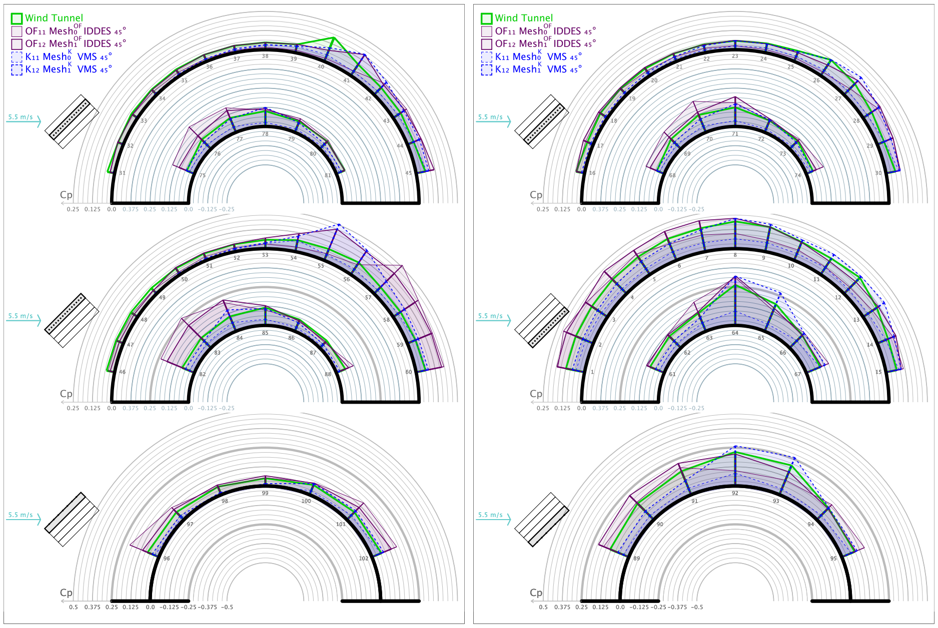

FIGURE 37. FVM-IDDES vs. FEM-VMS for mesh$_0$ and mesh$_1$ - standard deviation of C_p on all taps for 45° orientation [refer to Figure 26 for mean values].

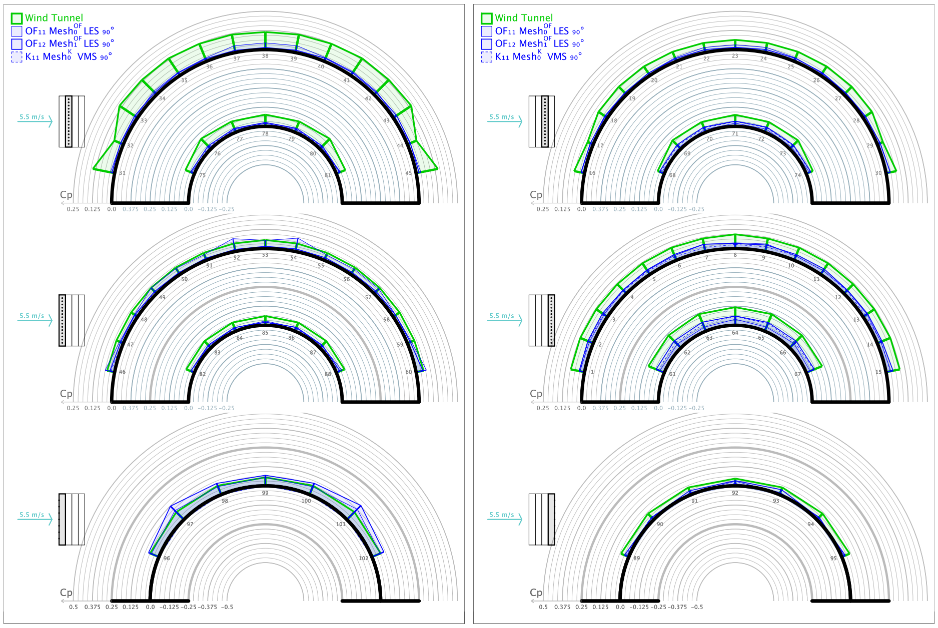

FIGURE 38. FVM-LES vs. FEM-VMS for mesh$_0$ and mesh$_1$ - standard deviation of C_p on all taps for 90° orientation [refer to Figure 27 for mean values].

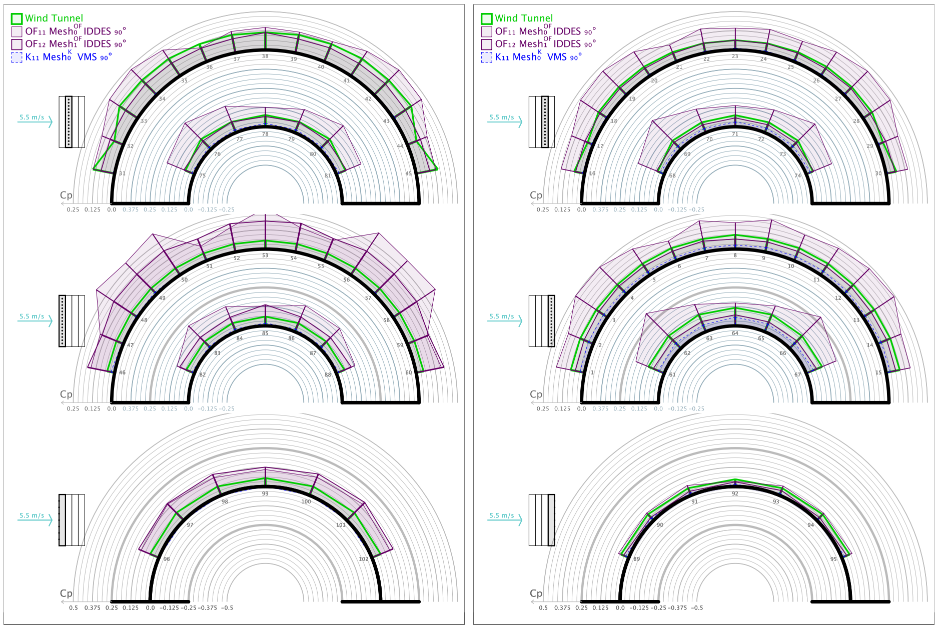

FIGURE 39. FVM-IDDES vs. FEM-VMS for mesh$_0$ and mesh$_1$ - standard deviation of C_p on all taps for 90° orientation [refer to Figure 28 for mean values].

Appendix B. **Discussion of the modeling assumptions.** Some simulations have been carried out to test the influence of the modeling assumptions adopted on the expected output. Some of which are listed below:

- *Slip boundary condition on the bottom.* Figure 40 shows the effect of adopting a slip boundary condition on the lower wall of the CFD computational domain when a uniform inflow is to be applied (as illustrated in section 3.1.2). A clear deviation from the reference data (i.e. the wind tunnel) can be observed when a no-slip condition is applied on the bottom wall boundary (these results are indicated in Figure 40 with a $*$). This is visible even on the taps at which capturing the physics of the flow is comparatively easy, i.e. the front part of the outer surface (e.g. taps n. 16,17 and 18).
- *Extended boxes.* Figure 41 shows the effect of extending Boxes 2 and 3 (see Figure 6) from the inlet to the outlet of the domain. The extension of the boxes does not improve the accuracy of the results and therefore can be avoided in order to reduce the computational effort. Figure 42 shows the effect of doubling the height and width of Boxes 2 and 3 in addition to extending them to the outlet. Similar to the previous point, enlarging those sub-domain meshing zones does not influence the results.
- *Variable time step during the simulation.* Figure 43 shows the effect of enlarging the time step from $\Delta t = 4e-5\,\mathrm{s}$ to $\Delta t = 2.5e-4\,\mathrm{s}$ after $0.5s$ of simulation (as illustrated in section 3.2.3). The increment on time step is done after the flow adjacent to the obstacle is converged to smaller magnitudes of velocity. This modification reduces the simulation time by a factor of 6 while keeping the same accuracy as shown in the figure.

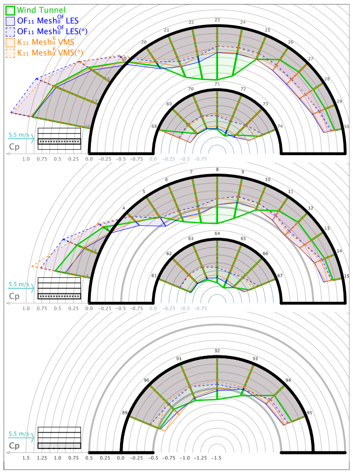

Figure 40. Comparison between slip (solid lines) and no-slip boundary condition (dotted lines with *) on the bottom wall

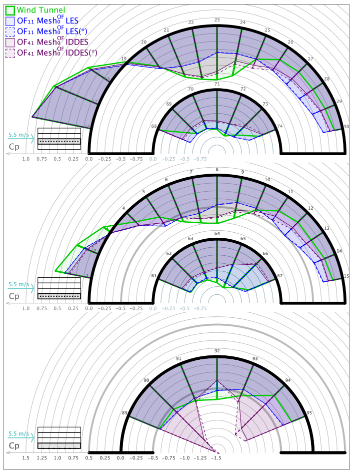

Figure 41. C_p results considering reduced or extended Boxes 2 and 3 (*).

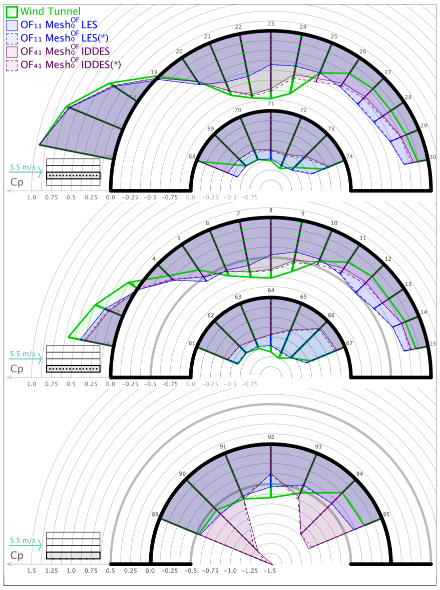

FIGURE 42. C_p results doubling the height and width of Boxes 2 and3 (*).

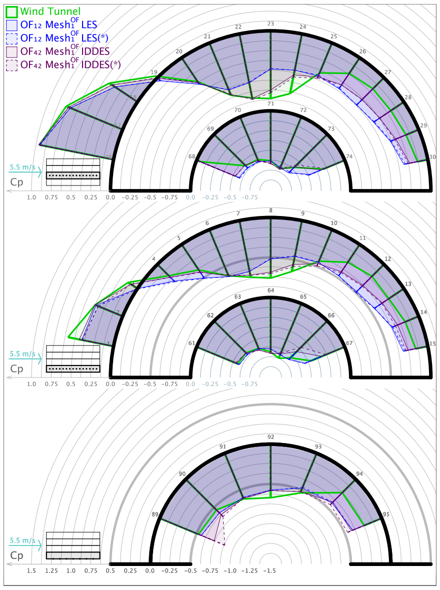

FIGURE 43. C_p results keeping the time step fixed (*) for the whole simulation.

REFERENCES

[1] F. Alauzet, B. Fabrèges, M. A. Fernández and M. Landajuela, Nitsche-xfem for the coupling of an incompressible fluid with immersed thin-walled structures, *Computer Methods in Applied Mechanics and Engineering*, **301** (2016), 300-335.

[2] M. Andre, M. Mier-Torrecilla and R. Wüchner, Numerical simulation of wind loads on a parabolic trough solar collector using lattice boltzmann and finite element methods, *Journal of Wind Engineering and Industrial Aerodynamics*, **146** (2015), 185-194.

[3] J. Bagget, On the feasibility of merging les with rans for the near-wall region of attached turbulent flows, In *In Annual Research Briefs. CTR, Stanford University*, (1998), 267-277.

[4] G. Bartoli, D. Allori, A. Giachetti and L. Pigolotti, Report on boundary layer wind tunnel tests on rigid and flexible models for uLites project, 2014.

[5] Y. Bazilevs, V. Calo, J. Cottrell, T. Hughes, A. Reali and G. Scovazzi, Variational multiscale residual-based turbulence modeling for large eddy simulation of incompressible flows, *Computer Methods in Applied Mechanics and Engineering*, **197** (2007), 173-201.

[6] B. Blocken, 50 years of computational wind engineering: Past, present and future, *Journal of Wind Engineering and Industrial Aerodynamics*, **129** (2014), 69-102.

[7] A. Bogaers, S. Kok, B. Reddy and T. Franz, Quasi-newton methods for implicit black-box fsi coupling, *Computer Methods in Applied Mechanics and Engineering*, **279** (2014), 113-132.

[8] R. Codina, Stabilized finite element approximation of transient incompressible flows using orthogonal subscales, *Computer Methods in Applied Mechanics and Engineering*, **191** (2002), 4295-4321.

[9] O. Colomés, S. Badia, R. Codina and J. Principe, Assessment of variational multiscale models for the large eddy simulation of turbulent incompressible flows, *Computer Methods in Applied Mechanics and Engineering*, **285** (2015), 32-63.

[10] J. Cotela-Dalmau, *Applications of Turbulence Modelling in Civil Engineering*, PhD thesis, Polytechnic University of Catalonia, 2016.

[11] J. Cotela-Dalmau, R. Rossi and E. Oñate, A fic-based stabilized finite element formulation for turbulent flows, *Computer Methods in Applied Mechanics and Engineering*, **315** (2017), 607-631.

[12] P. Dadvand, R. Rossi, M. Gil, X. Martorell, J. Cotela, E. Juanpere, S. Idelsohn and E. Oñate, Migration of a generic multi-physics framework to hpc environments, *Computers & Fluids*, **80** (2013), 301-309.

[13] P. Dadvand, R. Rossi and E. Oñate, An object-oriented environment for developing finite element codes for multi-disciplinary applications, *Archives of Computational Methods in Engineering*, **17** (2010), 253-297.

[14] E. de Villiers, *The Potential of Large Eddy Simulation for the Modeling of Wall Bounded Flows*, PhD thesis, Department of Mechanical Engineering, Imperial College of Science, Technology and Medicine, 2006.

[15] J. Degroote, K.-J. Bathe and J. Vierendeels, Performance of a new partitioned procedure versus a monolithic procedure in fluid-structure interaction, Fifth MIT Conference on Computational Fluid and Solid Mechanics, *Computers & Structures*, **87** (2009), 793-801.

[16] J. Degroote and J. Vierendeels, Multi-solver algorithms for the partitioned simulation of fluid-structure interaction, *Computer Methods in Applied Mechanics and Engineering*, **200** (2011), 2195-2210.

[17] C. Farhat and M. Lesoinne, Two efficient staggered algorithms for the serial and parallel solution of three-dimensional nonlinear transient aeroelastic problems, *Computer Methods in Applied Mechanics and Engineering*, **182** (2000), 499-515.

[18] M. A. Fernández, M. Landajuela and M. Vidrascu, Fully decoupled time-marching schemes for incompressible fluid/thin-walled structure interaction, *Journal of Computational Physics*, **297** (2015), 156-181.

[19] J. H. Ferziger and M. Perić, *Computational Methods for Fluid Dynamics*, Second revised edition. Springer-Verlag, Berlin, 1999.

[20] L. C. Foucard and F. J. Vernerey, An X-FEM-based numerical-asymptotic expansion for simulating a stokes flow near a sharp corner, *International Journal for Numerical Methods in Engineering*, **102** (2015), 79-98.

[21] J. Franke, A. Hellsten, H. Schlünzen and B. Carissimo, Best practice guideline for the CFD simulation of flows in the urban environment, *COST Action 732 Quality Assurance and Improvement of Microscale Meteorological Models*, 2007.

[22] P. Gousseau, B. Blocken and G. van Heijst, Quality assessment of large-eddy simulation of wind flow around a high-rise building: Validation and solution verification, *Computers & Fluids*, **79** (2013), 120-133.

[23] V. Gravemeier, The variational multiscale method for laminar and turbulent flow, *Archives of Computational Methods in Engineering*, **13** (2006), 249-324.

[24] W. Haase, M. Braza and A. Revell, *DESider (Detached Eddy Simulation for Industrial Aerodynamics)-A European Effort on Hybrid RANS-LES Modelling*, Springer, 2009.

[25] J. Hrvoje, *Error Analysis and Estimation for the Finite Volume Method with Application to Fluid Flows*, PhD thesis, Imperial College London, 1996.

[26] T. J. Hughes, Multiscale phenomena: Green's functions, the Dirichlet-to-Neumann formulation, subgrid scale models, bubbles and the origins of stabilized methods, *Computer Methods in Applied Mechanics and Engineering*, **127** (1995), 387-401.

[27] T. J. Hughes, G. R. Feijóo, L. Mazzei and J.-B. Quincy, The variational multiscale method-a paradigm for computational mechanics, *Computer Methods in Applied Mechanics and Engineering*, **166** (1998), 3-24. Advances in Stabilized Methods in Computational Mechanics.

[28] T. J. Hughes and J. R. Stewart, A space-time formulation for multiscale phenomena, *Journal of Computational and Applied Mathematics*, **74** (1996), 217-229.

[29] A. Kupzok, *Modeling the Interaction of Wind and Membrane Structures by Numerical Simulation*, PhD thesis, Technical University of Munich, 2009.

[30] R. Löhner, E. Haug, A. Michalski, B. Muhammad, A. Drego, R. Nanjundaiah and R. Zarfam, Recent advances in computational wind engineering and fluid-structure interaction, *Journal of Wind Engineering and Industrial Aerodynamics*, 144 (2015), 14-23.

[31] A. Michalski, B. Gawenat, P. Gelenne and E. Haug, Computational wind engineering of large umbrella structures, *Journal of Wind Engineering and Industrial Aerodynamics*, **144** (2015), 96-107. Selected papers from the 6th International Symposium on Computational Wind Engineering CWE, 2014.

[32] N. V. Nikitin, F. Nicoud, B. Wasistho, K. D. Squires and P. R. Spalart, An approach to wall modeling in large-eddy simulations, *Physics of Fluids*, **12** (2000), 1629-1632.

[33] S. Piperno, Explicit/implicit fluid/structure staggered procedures with a structural predictor and fluid subcycling for 2d inviscid aeroelastic simulations, *International Journal for Numerical Methods in Fluids*, **25** (1997), 1207-1226.

[34] T. Sawada and A. Tezuka, Llm and x-fem based interface modeling of fluid-thin structure interactions on a non-interface-fitted mesh, *Computational Mechanics*, **48** (2011), 319-332.

[35] M. L. Shur, P. R. Spalart, M. K. Strelets and A. K. Travin, A hybrid rans-les approach with delayed-des and wall-modelled les capabilities, *International Journal of Heat and Fluid Flow*, **29** (2008), 1638-1649.

[36] P. Spalart, W.-H. Jou, M. Strelets and S. R. Allmaras, Comments on the feasibility of les for wings, and on a hybrid rans/les approach, In *First AFOSR International conference on DNS/LES.*, (1997), 137-147.

[37] P. R. Spalart, S. Deck, M. L. Shur, K. D. Squires, M. K. Strelets and A. Travin, A new version of detached-eddy simulation, resistant to ambiguous grid densities, *Theoretical and Computational Fluid Dynamics*, **20** (2006), 181.

[38] D. B. Spalding, A single formula for the "law of the wall", *Journal of Applied Mechanics*, **28** (1961), 455-458.

[39] H. G. Weller, G. Tabor, H. Jasak and C. Fureby, A tensorial approach to computational continuum mechanics using object-oriented techniques, *Computers in Physics*, **12** (1998), 620-631.

[40] H. Werner and H. Wengle, Large-eddy simulation of turbulent flow over and around a cube in a plate channel, *Turbulent Shear Flows*, Berlin, Heidelberg, Springer Berlin Heidelberg, **8** (1993), 155-168.

[41] R. Wüchner, A. Kupzok and K.-U. Bletzinger, A framework for stabilized partitioned analysis of thin membrane-wind interaction, *International Journal for Numerical Methods in Fluids*, **54** (2007), 945-963.

[42] R. Zorrilla, R. Rossi, R. Wüchner and E. Oñate, An embedded finite element framework for the resolution of strongly coupled fluid-structure interaction problems. application to volumetric and membrane-like structures, *Computer Methods in Applied Mechanics and Engineering*, **368** (2020), 113179.

Received March 2023; revised March 2023; early access March 2023.